EURADCLIM: The European climatological high-resolution gauge-adjusted radar precipitation dataset

Aart Overeem[1], Else van den Besselaar[1], Gerard van der Schrier[1], Jan Fokke Meirink[1], Emiel van der Plas[1], and Hidde Leijnse[1]

[1]Royal Netherlands Meteorological Institute, Utrechtseweg 297, 3731 GA De Bilt, The Netherlands

Correspondence: Aart Overeem (overeem@knmi.nl)

Abstract. The European climatological high-resolution gauge-adjusted radar precipitation dataset, EURADCLIM, addresses the need for an accurate (sub-)daily precipitation product covering 78% of Europe at high spatial resolution. A climatological dataset of 1-h and 24-h precipitation accumulations on a 2-km grid is derived for the period 2013 through 2020. The starting point is the European Meteorological Network (EUMETNET) Operational Program on the Exchange of weather RAdar Information (OPERA) gridded radar dataset of 15-min instantaneous surface rain rates, which is based on data from, on average, 138 ground-based weather radars. First, methods are applied to further remove non-meteorological echoes from these composites by applying two statistical methods and a satellite-based cloud type mask. Second, the radar composites are merged with the European Climate Assessment & Dataset (ECA&D) with potentially ∼7700 rain gauges from National Meteorological and Hydrological Services (NMHS) in order to substantially improve its quality. Characteristics of the radar, rain gauge and satellite datasets are presented, as well as a detailed account of the applied algorithms. The clutter removal algorithms are effective, while removing few precipitation echoes. The usefulness of EURADCLIM for quantitative precipitation estimation (QPE) is confirmed by comparing against rain gauge accumulations employing scatter density plots, statistical metrics, and a spatial verification. These show a strong improvement with respect to the original OPERA product. The potential of EURADCLIM to derive pan-European precipitation climatologies and to evaluate extreme precipitation events is shown. Specific attention is given to remaining artefacts in and limitations of EURADCLIM. Finally, it is recommended to further improve EURADCLIM by applying algorithms to 3D instead of 2D radar data, and by obtaining more rain gauge data for the radar-gauge merging. The EURADCLIM 1-h and 24-h precipitation datasets are publicly available at https://doi.org/10.21944/7ypj-wn68 (Overeem et al., 2022a) and https://doi.org/10.21944/1a54-gg96 (Overeem et al., 2022b).

1 Introduction

Accurate surface precipitation information at high spatiotemporal resolutions is needed for many scientific domains and applications, such as agriculture, water management, weather prediction and climate monitoring, but is often lacking. EUMETNET (European Meteorological Network) is a network of 31 National Meteorological and Hydrological Services (NMHS) and one of its programs is OPERA (Operational Program on the Exchange of weather RAdar information). In OPERA, expertise on operational ground-based weather radars is exchanged and pan-European radar products have been developed, which are dis-

seminated in near real-time (Huuskonen et al., 2014; OPERA, 2022). While the EUMETNET OPERA ground-based weather radar composite provides strong coverage at the km scale, it generally underestimates precipitation by tens of percent. The spatial variability of this bias indicates that its quality is inhomogeneous in time and space. Moreover, many smaller areas suffer from severe overestimation due to non-meteorological echoes (clutter), mainly due to signal interference (Saltikoff et al., 2016), obstacles in the vicinity of radars, and refraction of the radar beam (e.g. Gourley et al., 2007; Fabry, 2015; Overeem et al., 2020). A long list of possible sources of error can negatively affect radar precipitation estimates (Doviak and Zrnić, 1993; Fabry, 2015; Rauber and Nesbitt, 2018; Ryzhkov and Zrnic, 2019): for instance, hardware-related errors such as electronic calibration and antenna pointing offsets (Frech et al., 2017), and severe underestimation due to rain-induced attenuation along the radar beam for X- or C-band radars (e.g. Hitschfeld and Bordan, 1954; Tabary et al., 2009; Jacobi and Heistermann, 2016; Overeem et al., 2021). Another source of error are, for instance, changes in the vertical profile of reflectivity, where the height of the radar sampling volume increases with increasing range from the radar, hence becoming less representative for the reflectivity at the ground (Hazenberg et al., 2013). In contrast, rain gauges often provide accurate local quantitative precipitation estimation (QPE), but their network densities are usually too sparse to capture the spatial precipitation variability, especially at the sub-daily time scale (Van de Beek et al., 2012). Gridded precipitation datasets based on interpolated gauge accumulations and covering large parts of Europe, provide at best daily accumulations at 0.1° and 0.25° grids (Cornes et al., 2018).

A common practice on a national level is to combine the best of two worlds by merging radar with rain gauge data (e.g. Holleman, 2007; Goudenhoofdt and Delobbe, 2016; Nelson et al., 2016; Fabry et al., 2017; Bližňák et al., 2018; Winterrath et al., 2018; Barton et al., 2020). For Europe, Park et al. (2019) developed an operational gauge-adjusted OPERA-based radar rainfall product for the European Rainfall-InduCed Hazard Assessment (ERICHA) system, ~~employing data from ~1500 rain gauges~~. This is used to compute flash flood hazard for Europe for the next ~~5~~ 6 hours for the European Flood Awareness System (EFAS). ~~The use of this dataset is restricted to EFAS.~~

Here, we present an open climatological OPERA-based radar precipitation product over the period 2013–2020, called EURADCLIM (EUropean RADar CLIMatology). It covers $\sim 8 \times 10^6$ km^2 of Europe, which is about 78% of geographical Europe, and covers a variety of climates from Mediterranean to temperate, mountain, continental and arctic. Some differences with the study by Park et al. (2019), who developed a (near) real-time dataset, are that additional algorithms to remove non-meteorological echoes are applied, and data from far more rain gauges are available (after waiting 1.5 years (at most ~7700 instead of at most a few thousand). In addition, for each 1-hour interval that is adjusted, the corresponding gauge data are used to compute a spatial adjustment factor field for that hour, instead of applying such a field based on radar and gauge data from the last 7 rainy days, as is the case in the Park et al. (2019) dataset. In EURADCLIM, non-meteorological echoes are further removed by applying an open-source statistical filter taking into account large gradients and the size of contiguous echoes (Gabella and Notarpietro, 2002; Wradlib, 2021). ~~Since it could also~~ The Gabella clutter filter does not depend on historical or auxiliary data and could be applied in (near) real-time, ~~its evaluation~~. Hence, evaluation of its performance to remove non-meteorological echoes is also relevant for the existing gridded OPERA products. Next, a climatological satellite cloud type product is employed to identify areas with semitransparent clouds or without clouds, and set rain rates to 0 mm

h^{-1} in those areas. Finally, for each year a static clutter mask is computed based on outliers in annual precipitation. For these locations, 1-h radar precipitation accumulations are replaced by spatially interpolated values. Merging these radar precipitation accumulations with those from rain gauges, results in EURADCLIM, which can be seen as the continental European analogue of a climatological radar precipitation dataset developed for the United States (Fabry et al., 2017). Having 24-h accumulations can, for instance, be useful for evaluation of extreme precipitation events, evaluation of EURADCLIM against (manual) rain gauge accumulations, and climatological analyses. Moreover, the ETCCDI Climate Indices require daily precipitation amounts for climate monitoring (https://www.wcrp-climate.org/etccdi). In addition, a drawback of the gridded E-OBS dataset is that the underlying rain gauges are aggregated over daily measurement intervals that are not homogeneous over Europe. The unique nature of EURADCLIM improves upon this aspect. Hence, the EURADCLIM dataset is not only available as 1-h, but also as 24-h accumulations.

The outline of this paper is as follows: First, characteristics of the employed radar, rain gauge and satellite datasets, such as data availability and coverage, are described (Sect. 2). Next, the three algorithms to remove non-meteorological echoes and the radar-gauge merging algorithm are presented (Sect. 3). This is followed by a step-by-step evaluation of the datasets after each processing step, including the EURADCLIM dataset, against rain gauge data (Sect. 4.1–4.2). EURADCLIM's limitations are discussed and illustrated together with pan-European precipitation climatologies (Sect. 4.3). The results section ends with extreme precipitation events derived from EURADCLIM (Sect. 4.4). Finally, conclusions and recommendations to improve EURADCLIM are provided (Sect. 5).


2 Data

2.1 OPERA radar data

The radar composite product "instantaneous surface rain rate" was obtained from the EUMETNET OPERA Data Centre (ODC or Odyssey) from the period 2013–2020. It is stored in Hierarchical Data Format version 5 (HDF5) files employing the OPERA Data Information Model (ODIM) (Michelson et al., 2019). This product has a temporal resolution of 15 min and a spatial resolution of 2 km × 2 km (Lambert Azimuthal Equal Area projection; 2200 × 1900 grid cells). As is usually the case for gridded radar precipitation products, the effective resolution decreases for increasing distances from radars and will become lower than 4 km^2 (typically at ~ 115 km from a radar for a beam width of $1°$). It is based on the raw 3D single site radar data from NMHS, which have undergone Doppler clutter filtering. The latter helps to detect and correct for clutter in case the radial Doppler velocity is (near) zero. Hence, the influence of (nearly) stationary targets on radar reflectivity factors is diminished, while preserving the non-stationary precipitation targets. Depending on the radar, beam-blockage correction and additional (dual-polarization) clutter filtering have been applied by the respective NMHS. OPERA applies algorithms on either individual radar data or the composite, concerning further removal of non-meteorological echoes and, since late 2015, beam-blockage correction and a satellite cloud mask to remove non-meteorological echoes (Saltikoff et al., 2019b).

The number of contributing radars, on average 138 based on intervals with data, gradually increases over the period 2013–2020 (Fig. 1a). A variety of radars is employed, for instance, different manufacturers, different frequencies (mostly C-band,

some X-band and S-band) and a mixture of single-polarization and dual-polarization radars. The measurement frequency of the radars is 5 min or 10 min, and data from the last time stamp are used in the composite product, ~~e. g.~~ For instance, the 5-min file from 10:15 UTC and the 10-minute file from 10:10 UTC for the 10:15 UTC OPERA composite product. The lowest elevation scan data from all radars are combined to produce a composite of gridded horizontally polarized radar reflectivity factor (Z_{h}) data. Before 29 Sep 2017 08:52 UTC, this was done via logarithmic range-weighted averaging (dBZ_{h}) and afterwards via linear range-weighted averaging (Z_{h}). Finally, instantaneous surface rain rates are retrieved from the reflectivity composites every 15 min using the Marshall-Palmer $Z_{\mathrm{h}} - R$ relation ($Z_{\mathrm{h}} = 200R^{1.6}$). Saltikoff et al. (2019b) provide more details on the OPERA radar data and its processing.
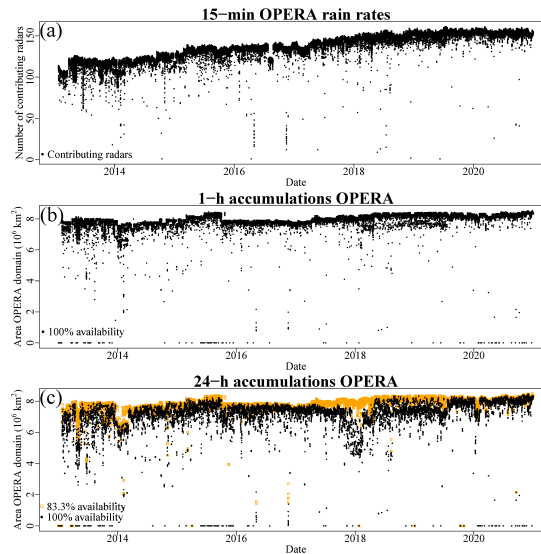
Figure 1. OPERA radar data availability as a function of time over the period 2013–2020. (a) Number of contributing radars to the OPERA composite of rain rates in case data are available for at least part of the OPERA domain. Coverage of OPERA radar datasets as a function of time for the (b) 1-h and (c) 24-h precipitation accumulations. For (b) and (c) also time intervals without data are plotted (as 0).

For each radar grid cell (pixel) and clock-hour (i.e., every hour on the hour), 1-h precipitation accumulations are computed from the rain rates in case of full availability, otherwise the grid cells contain the ODIM "nodata" value, which is "used to denote areas void of data (never radiated)" (Michelson et al., 2019). So, 1-h accumulations are only derived if all 15-min OPERA rain rates are not equal to the "nodata" value. And "undetect" values from the OPERA rain rates, "used to denote areas below the measurement detection threshold (radiated but nothing detected)" (Michelson et al., 2019), are set to 0 mm. These 1-h precipitation accumulations are used to compute 24-h accumulations every clock-hour as well as annual accumulations. For each radar grid cell, a minimum data availability of underlying 1-h accumulations of 83.3% is demanded (i.e., at least 20 of 24 hours, or ∼304.2 of 365 days). Grid cells with too low availability are set to the OPERA "nodata" value. The availability of 1-h and 24-h precipitation accumulations is generally high (Fig. 1b–c). For the large majority of the OPERA domain, availability of 1-h precipitation accumulations is at least 95% over the period 2013–2020 (Fig. 2a). The distance to the nearest radar displays

quite some variability, but is generally shorter than 175 km (Fig. 2c). The median and mean distance to the nearest radar is 110 km and 133 km, respectively. Some countries do have radars but these do not contribute to the OPERA composite yet (e.g., Austria and Italy). All derived radar datasets are kept in ODIM-HDF5 format on the default OPERA grid of 2 km resolution.
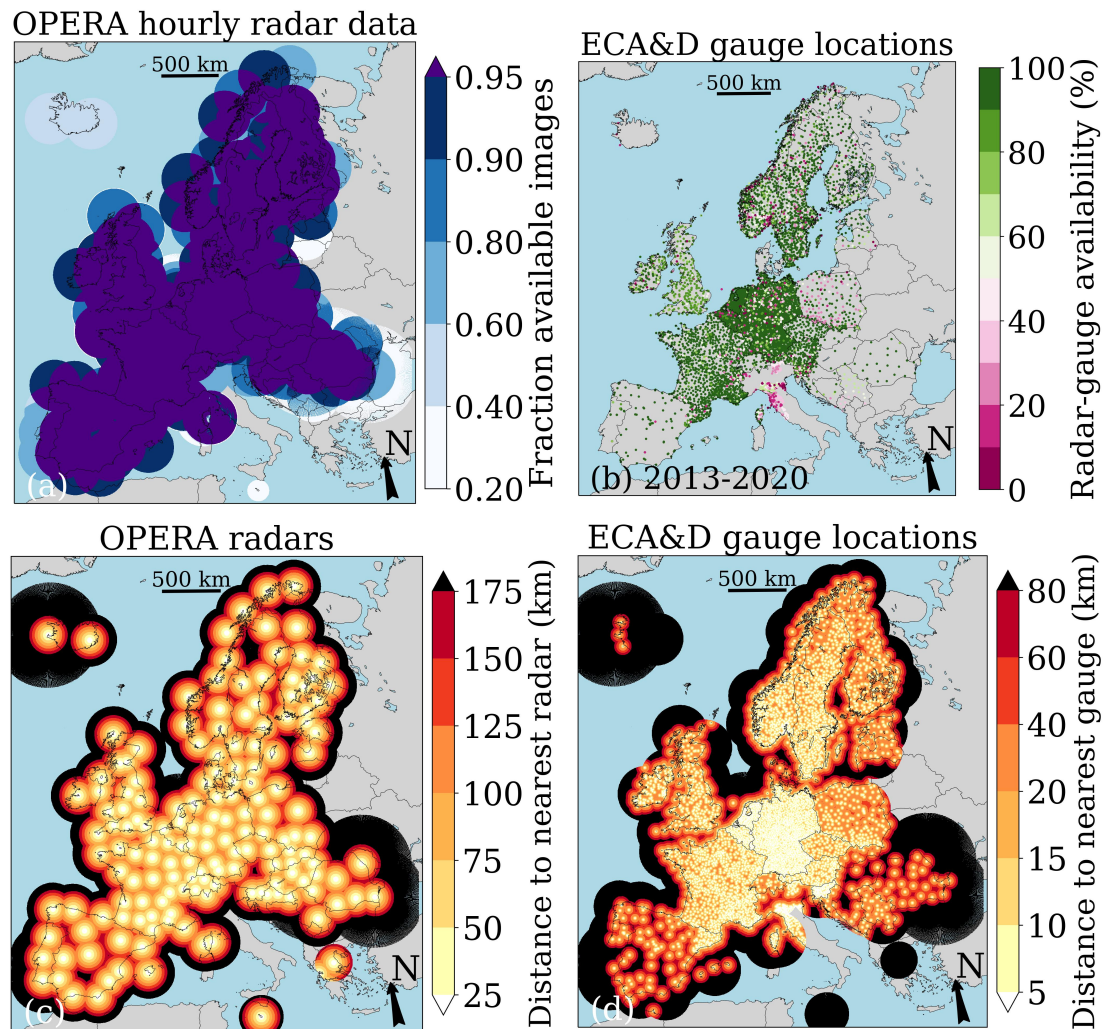
Figure 2. (a) Map of the OPERA domain with fraction of available radar composites over the period 2013–2020. (b) Map with combined radar-gauge availability over the period 2013–2020. (c) Map of distance to nearest radar per grid cell assuming full availability of radar data (note that some of the radars only contributed part of the period). (d) Map of distance to nearest rain gauge per grid cell assuming full availability of radar and gauge data. This shows the best possible result. In reality, the average minimum distance will be longer because sometimes gauge data are missing. Maps made with Natural Earth. Free vector and raster map data ©naturalearthdata.com.

2.2 ECA&D and E-OBS rain gauge data

115 Daily precipitation series were obtained ~~mid June 2022~~ from the European Climate Assessment and Dataset (ECA&D, https://www.ecad.eu) project (Klein Tank and coauthors, 2002; Klok and Klein Tank, 2008). In total, $\sim$7700 rain gauges from 29 different countries and 37 different data providers, including non-downloadable series (i.e., included in ECA&D for production of derived data but only accessible through the data-owning NMHS), are covered by OPERA radars during (part of) the 2013–2020 period. Combined radar-gauge data availability is at least 90% for most regions (Fig. 2b). This availability is the

120 percentage of daily intervals in the 8-year period at each gauge location where the gauge and corresponding radar accumulations are both available. Figure 2d displays the distance to the nearest gauge for the OPERA domain if all $\sim$7700 gauges would be available. The large variability in space of the underlying rain gauge network density is obvious. The median and mean distance to the nearest rain gauge is 42 km and 92 km, respectively. These relatively long distances are mainly caused by areas above land surface with low rain gauge network densities, and above sea. The ECA&D rain gauge dataset will be used to evaluate the

125 various radar precipitation datasets and will be merged with 1-h radar accumulations.

The rain gauge data have undergone quality control by the ECA&D team (Project team ECA&D, Royal Netherlands Meteorological Institute KNMI, 2021) and often by NMHS. Given the latency in gauge data provided to ECA&D for some networks and to prevent spatial differences in the quality of merged radar-gauge QPE, only data up to and including 2020 are used. At the time of data production (mid June 2022) it was found for some countries that the density of gauge networks from which

130 data were available is relatively sparse (Bosnia and Herzegovina, Croatia, Denmark, Hungary, Iceland, Lithuania, Portugal, Romania, Slovakia, Spain, Switzerland), no data are available (e.g., Bulgaria, Greece, Kosovo, North Macedonia) or not complete for the entire period (e.g., for Romania it ends 31 September 2020, for Serbia it ends 31 December 2017, only a few years for Montenegro, and time series from most stations in the United Kingdom end 31 December 2019).

The daily measurement interval of gauges is often not exactly known to ECA&D. For instance, the metadata for some

135 networks is imprecise as aggregation intervals ending at 06:00, 07:00 or 08:00 UTC are lumped together. Sometimes, additional information on the measurement interval end time from the respective NMHS was available and selected. In order to determine the exact measurement interval for other gauge networks, gauge accumulations are compared to OPERA 24-h accumulations by testing different measurement interval end times. For each network, distributions of Pearson correlation coefficients for all gauge locations are evaluated for each interval end time using Ridgeline plots. The measurement interval end time with the

140 highest correlations is selected for that given network. The end times of the observations display a large variability across Europe from 0 UTC (9 networks), 6 UTC (16 networks), 6 UTC in summer and 7 UTC in winter (1 network), 7 UTC (1 network), 8 UTC (3 networks), 9 UTC (2 networks), 18 UTC (3 networks), 21 UTC (1 network), to 22 UTC in summer and 23 UTC in winter (1 network).

A pan-European dataset, E-OBS version 25.0e (https://surfobs.climate.copernicus.eu/dataaccess/access_eobs.php#datafiles),

145 of gridded, daily, interpolated ECA&D gauge accumulations (Cornes et al., 2018) is used to compute annual precipitation accumulations. These will be used for comparison with EURADCLIM accumulations.
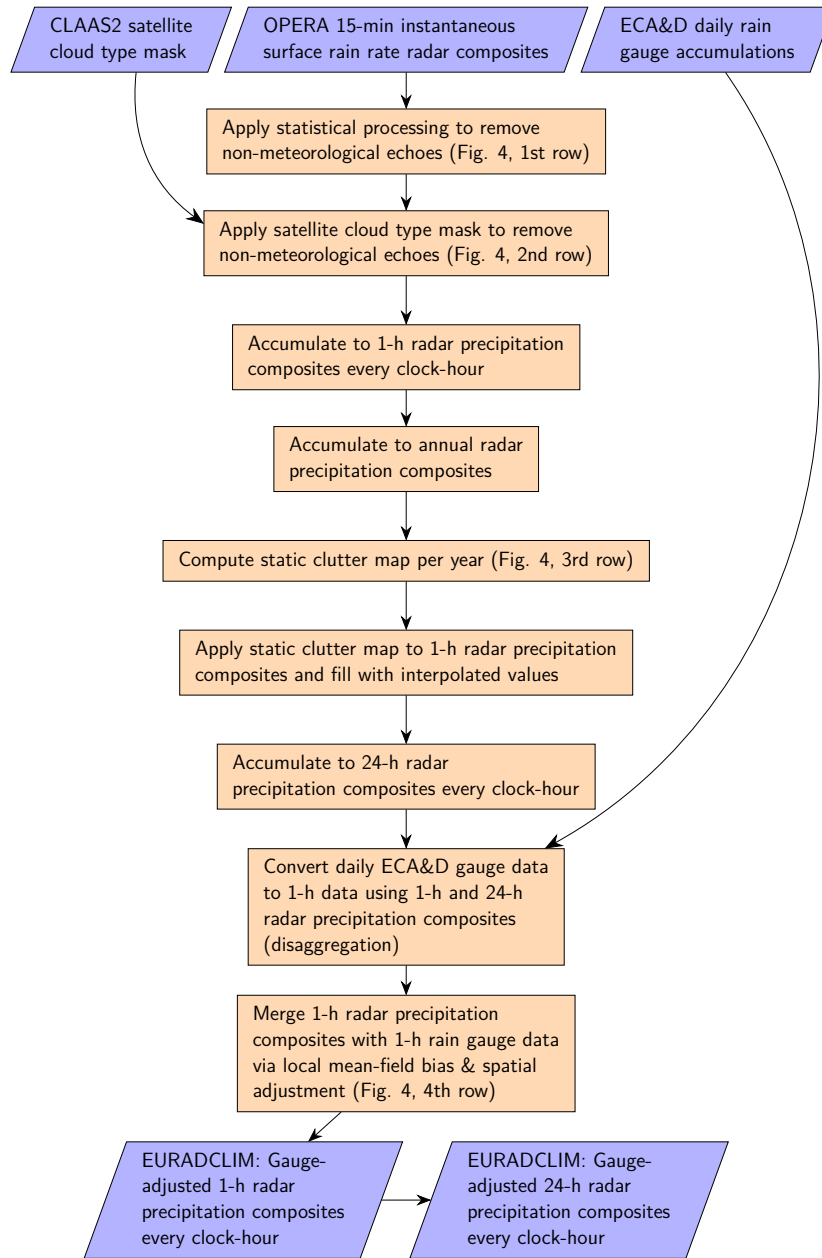
2.3 Satellite cloud type product

Information on the occurrence and type of clouds was obtained from the Spinning Enhanced Visible and Infrared Imager (SE-VIRI) onboard the geostationary Meteosat Second Generation (MSG) satellites operated by the European Organisation for the Exploitation of Meteorological Satellites (EUMETSAT). The CLoud property dAtAset using SEVIRI edition 2 (CLAAS-2) was used, produced by EUMETSAT's Satellite Application Facility on Climate Monitoring (CM SAF). CLAAS-2 (Finkensieper et al., 2016; Benas et al., 2017) is a climate data record of cloud properties derived from SEVIRI measurements and extending from 2004 to present. The CLAAS-2 cloud type product was derived with the MSGv2012 software package developed by the SAF on Nowcasting and Very Short Range Forecasting (NWC SAF). Further details on the retrieval algorithm can be found in Derrien and Le Gléau (2005) and NWC SAF (2013). The temporal resolution of CLAAS-2 is 15 minutes. Its spatial resolution is 3 km × 3 km at the sub-satellite point and around 4 km × 7 km in the centre of the OPERA domain ($\sim 52°$ N). The cloud type was converted from the CLAAS-2/SEVIRI grid to the native OPERA radar grid of 2 km by 2 km using nearest neighbour resampling. This dataset is available day and night and is used to remove non-meteorological echoes from the OPERA radar data. Over the period 2013-2020, 99.7% of the 15-min intervals have valid data.

3 Methodology

The flowchart in Fig. 3 provides an overview of the input datasets, the applied processing, and the output dataset EURADCLIM. Three algorithms are applied to further remove non-meteorological echoes from the OPERA radar data. Finally, the radar data are merged with the ECA&D rain gauge data.

3.1 Gabella clutter filter

The function *clutter.gabella* from the open-source Python library for weather radar data processing wradlib version 1.9.0 (Heistermann et al., 2013; Mühlbauer et al., 2020) is employed to classify non-meteorological echoes. This Gabella filter is a two-part algorithm (Gabella and Notarpietro, 2002; Wradlib, 2021), which uses as input the radar reflectivity factors. For this, rain rates are converted to radar reflectivity factors employing $Z_\mathrm{h} = 200R^{1.6}$ (beforehand "undetect" and "nodata" values are set to 0 mm h^{-1}). Then the Gabella filter is used to classify grid cells using the Cartesian radar reflectivity factor data. In the first part of the filter, strong spatial gradients are identified by checking for each grid cell how many cells surrounding it in a square lattice of 5×5 cells are less than 6 dBZ_h lower than the central cell. When this number of cells is lower than 6, the central cell is identified as clutter. In the second part of the filter, the ratio between the area and circumference for contiguous echo regions is computed, where these consist of cells with a value above 0 dBZ_h. When the absolute value of this ratio is lower than 1.3, the central cell is identified as clutter. Next, the original surface rain rates are set to 0 mm h^{-1} in case one or two of the parts of the Gabella filter identify clutter. Central cells that have "nodata" values in the original rain rates are unaffected by the Gabella filter, and "undetect" values are kept in case of no clutter. A successful example of applying the Gabella clutter filter for the Netherlands and surroundings is provided in Fig. 4a–b.

Figure 3. Flowchart of radar and gauge data processing for EURADCLIM.

### 3.2 Satellite cloud type mask clutter filter

A satellite cloud type mask is employed to classify remaining non-meteorological echoes. Localisation errors (e.g., advection, timing differences between radar and satellite, parallax) are taken into account by considering all grid cells in a square lattice

of 7×7 cells containing the central cell for which the classification is performed. The rain rate for this central cell is set to 0 mm h^{-1} when all cells in the square lattice are either classified as cloud-free or as containing semitransparent clouds (which are assumed to be non-raining). Concretely, these cases correspond to the following MSGv2012 cloud type categories: cloud free land, cloud free sea, land contaminated by snow, sea contaminated by snow/ice, high semitransparent thin clouds, high semitransparent meanly thick clouds, and high semitransparent thick clouds. In case satellite data is not available for a given pixel (category "non-processed containing no data or corrupted data" or no file/image available), that pixel is not used as a neighbouring pixel and the radar pixel directly beneath it will not be labelled as clutter. Figure 4c–e illustrates the working of this algorithm by providing a 15-min radar rain rate, before and after applying the satellite cloud type mask, which is also displayed. Because the satellite images are referenced to with the start time of observation and the radar composites are referenced to with the end time of observation, a satellite image of, for example, 12:00 UTC is combined with the radar composite of 12:15 UTC.

3.3 Static clutter filter

The 15-min radar rain rates are accumulated to 1-h and these to annual precipitation accumulations. The function *clutter.histo_cut* from the open-source Python library for weather radar data processing wradlib version 1.9.0 (Heistermann et al., 2013; Mühlbauer et al., 2020; Wradlib, 2022) is employed to classify non-meteorological echoes in the annual precipitation accumulation. First, a histogram of 50 classes is computed from the annual precipitation from a given year using all grid cells. Next, the class with the largest frequency is determined. An iterative procedure detects those classes with a frequency below 5% of the frequency of the class with the largest frequency (the hard-coded default value is 1%). The procedure stops when the changes in the maximum annual rainfall from the remaining classes becomes (smaller than) 1 mm compared to the previous iteration. The grid cells corresponding to the detected classes become the static clutter mask. For each year a separate static clutter mask is obtained. This algorithm identifies areas with static clutter and may also detect areas affected by ~~beam-blockage~~beam blockage. Next, inverse distance weighted interpolated values are computed for the identified grid cells (inverse distance weighting power of 2; maximum of 4 neighbours). This value replaces the original value only in case it is lower than the original value. The original "nodata" values are kept in the output dataset. The interpolation is performed on the 1-h precipitation accumulations. From the cleaned 1-h accumulations, which are used for merging with rain gauge accumulations, 24-h accumulations for every clock-hour are derived. Figure 4f–h shows an example of an annual precipitation accumulation, the derived annual precipitation accumulations after applying the static clutter mask including interpolation on the underlying 1-h radar precipitation composites, and the corresponding static clutter mask. The mask seems to correspond mostly to areas with high annual precipitation. In theory, the interpolation could decrease precipitation estimates for areas with ~~beam-blockage~~beam blockage. Areas with ~~beam-blockage~~ beam blockage are not abundant, though. Also note that a beam-blockage correction has already been applied by OPERA.
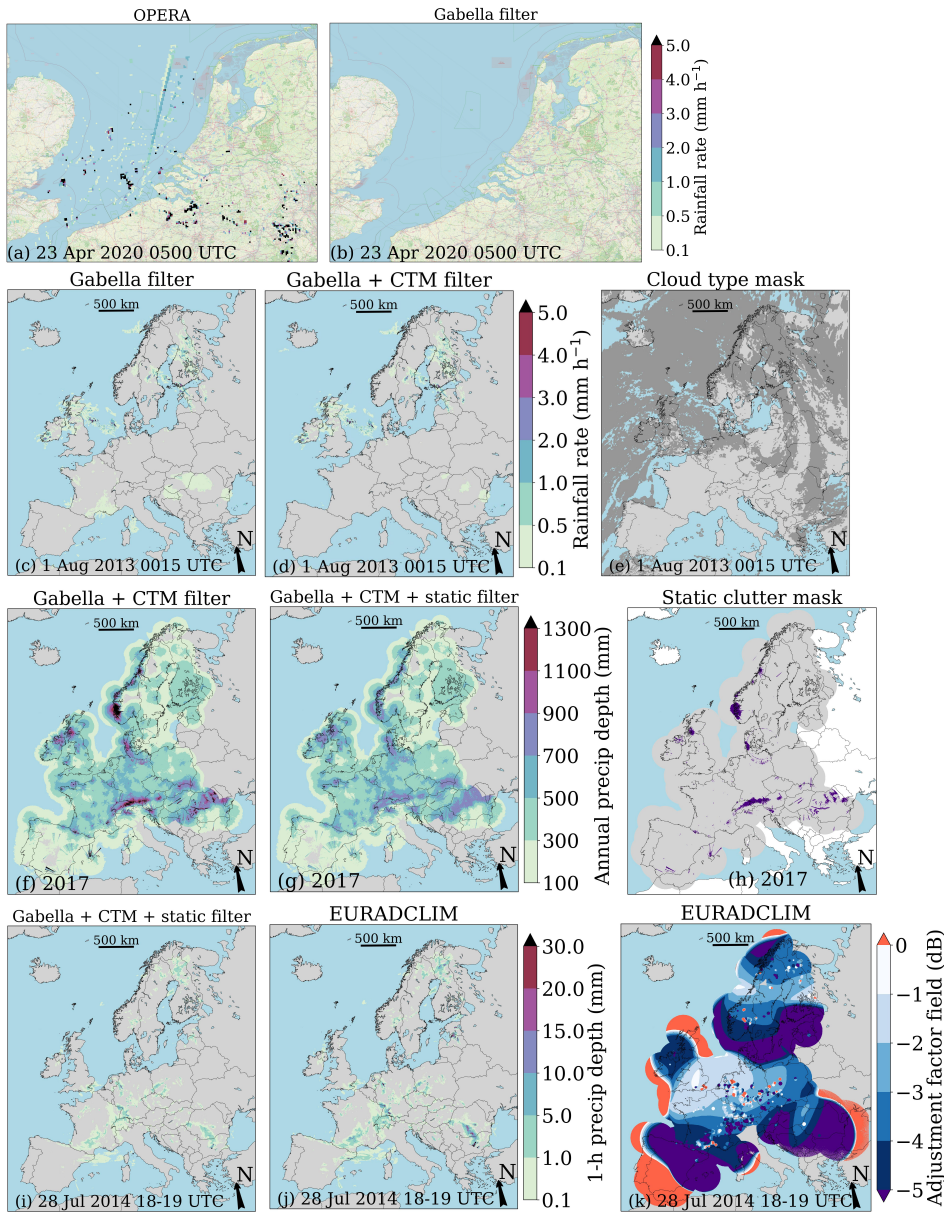
Figure 4. Illustration of application of all three clutter removal steps and the rain gauge adjustment, i.e., of all processing steps in EU-RADCLIM. (a)–(b) Application of the Gabella clutter filter (map data ©OpenStreetMap contributors 2022. Distributed under the Open Data Commons Open Database License (ODbL) v1.0), and of (c)–(e) the cloud type mask to remove non-meteorological echoes from a 15-min OPERA composite of rain rates. For the cloud type mask, the grey areas indicate where the cloud type does not belong to the seven categories listed in Sect. 3.2, and for which the radar rain rates were thus left untouched. (f)–(h) Illustration of application of the static clutter mask, derived from the annual precipitation map, to 1-h radar precipitation composites, which are accumulated to an annual precipitation map. (i)–(k) Application of the radar-gauge merging algorithm going from unadjusted to adjusted 1-h rainfall accumulations employing the 1-h adjustment factor field. (c)–(k) Maps made with Natural Earth. Free vector and raster map data ©naturalearthdata.com.

3.4 Merging radar with ECA&D rain gauge data

Starting point of the merging algorithm is that radar and rain gauge data are used from the same 1-h interval, instead of computing adjustment factor fields based on preceding time intervals, such as in Park et al. (2019). Since the measurement interval of daily rain gauge accumulations varies across Europe, a daily adjustment factor field would not be entirely representative. And since the aim is to derive 1-h adjusted radar precipitation accumulations, ideally, 1-h adjustment factor fields would be computed. To achieve this, the daily gauge accumulations are disaggregated to 1-h accumulations employing the 1-h and 24-h radar accumulations from the previous processing step. The end times of the observations, as determined in Section 2.2, are taken into account in the disaggregation. It is assumed that the gauges observed precipitation only during the intervals for which radar data were available. So in case of missing radar data, at most 4 hours per 24-h interval, the daily gauge precipitation is only distributed over the remaining (at least 20) hours. The threshold of 4 hours comes from the minimum required availability of 83.3% to aggregate 1-h to 24-h radar accumulations. If this requirement is not met for a given radar grid cell and 24-h interval, the "nodata" value is assigned to the radar grid cell. Hence, if more than 4 hours of radar data at the location of a rain gauge are missing per 24 h, the disaggregation to 1-h gauge values cannot be performed. The merging of 1-h disaggregated rain gauge data and radar data is simply performed with all available radar-gauge pairs. If no radar-gauge pairs would be available at all, due to either missing radar (i.e., only "nodata" values at gauge locations) or rain gauge data, the merging is not performed, and EURADCLIM will be a copy of the unadjusted radar dataset. Next, to decrease computation time of the radar-gauge merging, only 1-h radar-gauge pairs for which gauge precipitation exceeds 0.25 mm are used for merging. This is expected to have limited effect on the quality of the merged dataset.

The radar-gauge merging algorithm is based on Barnes' Objective Analysis (Barnes, 1964) but has been extended to make it robust in case of sparse gauge network densities for short durations (1 h), when spatial precipitation variability is often large. A spatial adjustment factor field F_c is computed from the distance-weighted interpolation of the raw radar precipitation accumulations ($S_{w,r}$) and the interpolation of the corresponding gauge precipitation accumulations ($S_{w,g}$), implying that it is computed for each radar grid cell, which has position (x, y):

$$
F_c(x,y) = \begin{cases}
\frac{S_{w,r}}{S_{w,g}} & \text{if} \quad S_{w,r} > T \bigvee S_{w,g} > T \\
\frac{T}{S_{w,g}} & \text{if} \quad S_{w,r} \leq T \bigvee S_{w,g} > T \\
\frac{S_{w,r}}{T} & \text{if} \quad S_{w,r} > T \bigvee S_{w,g} \leq T \\
1 & \text{if} \quad S_{w,r} \leq T \bigvee S_{w,g} \leq T,
\end{cases}
\tag{1}
$$

with T a threshold value of 0.25 mm. $S_{w,X}$, with X an indicator being g (gauge) or r (radar), is defined as:

$$
S_{w,X} = \sum_{n=1}^{N_P} w_n R_{X,n},
\tag{2}
$$

which is computed over N_P radar-gauge pairs. $R_{r,n}$ and $R_{g,n}$ are the precipitation accumulations at the gauge location n for radar and gauge, respectively. In case the value of $S_{w,X}$ is below T, it is set equal to T. This is done to prevent outliers in the gauge-adjusted radar precipitation accumulations. The weighting function w_n depends on the distance of a grid cell to the

gauge location:

$$w_n = \frac{G_\mathrm{w}\left(n, r_\mathrm{s}\right) + v \cdot G_\mathrm{w}\left(n, r_\mathrm{l}\right)}{1 + v}, \tag{3}$$

where $G_\mathrm{w}\left(n, r_\mathrm{d}\right)$ is a Gaussian function:

$$G_\mathrm{w}\left(n, r_\mathrm{d}\right) = \begin{cases} \frac{\exp\left(-4\frac{(x-x_n)^2+(y-y_n)^2}{r_\mathrm{d}^2}\right) - \exp(-4)}{1 - \exp(-4)} & \text{if} \quad (x-x_n)^2 + (y-y_n)^2 \leq r_\mathrm{d} \\ 0 & \text{if} \quad (x-x_n)^2 + (y-y_n)^2 > r_\mathrm{d}, \end{cases} \tag{4}$$

245 and (x_n, y_n) the position of gauge n. Equation 3 employs two Gaussian functions, each with its own characteristic distance r_d for which the influence of a gauge is reduced to 0. The shorter range, r_s, results in a local adjustment in the neighbourhood of gauges. The value of r_s is taken as the range of an isotropic spherical variogram model, which has been expressed as a function of day of year (DOY) and duration (1–24 h) using a 30-year rain gauge dataset from the Netherlands from the period 1979–2009 (Van de Beek et al., 2012). When distances from a grid cell to gauges are longer than r_s, this short range component

250 does not contribute to the adjustment. The longer range, r_l, set at 500 km, is used to also adjust when gauge network density is sparse and the nearest gauges are far away (e.g., over sea). The value of v controls the contribution of this long range component with respect to the short range component. Apart from the actual adjustment in which all selected gauges are used, leave-one-out-statistics (LOOS) are also provided. These statistics are computed based on adjusted radar precipitation accumulations computed for a given gauge location without using that particular gauge in the adjustment. This is repeated for each gauge

255 location, thus allowing for an independent verification of the gauge-adjusted radar dataset.

The algorithm can also run two adjustments consecutively with different settings, while still providing LOOS. Here, first an adjustment is performed with $v = 100000$, implying a local mean-field bias adjustment taking into account all gauges within a radius of 500 km. The short range component does not play a role then. This helps to remove systematic underestimations as much as possible in regions with low gauge network densities. Tests indicated that underestimations could not be effectively

260 removed when also the short range component contributed. Next, v is set to 0, implying that only a local spatial adjustment is performed on top of the already mean-field bias adjusted precipitation estimates. The adjustment factor fields from both adjustments are combined into one 1-h spatial adjustment factor field. The 1-h radar precipitation composite is divided by this adjustment factor field to obtain the 1-h adjusted radar precipitation composite (EURADCLIM). Figure 4i–k illustrates the adjustment by showing an unadjusted radar composite, the adjusted radar composite and the adjustment factor field. The effect

265 of the long and short range components is visible in the adjustment factor field, where the large-scale patterns belong to the long range component ($v = 100000$) and the local patterns (dots) show the influence of the short range component ($v = 0$) on top of the long range component.

3.5 Evaluation

The radar precipitation accumulations are evaluated against rain gauge accumulations by means of scatter density plots, maps

270 with station-based spatial verification, comparison of annual precipitation maps to those based on gridded rain gauge data (E-OBS), and statistical metrics. In addition, maps of the mean hourly precipitation and the relative frequency of exceeding

a threshold value of 1-h precipitation are compared between different processing steps. Statistical metrics used for evaluation are the relative bias of radar precipitation accumulations compared to the corresponding gauge precipitation accumulations, the residual standard deviation divided by the mean gauge precipitation accumulation (i.e., the coefficient of variation, CV), the Pearson correlation coefficient (ρ) and the mean absolute error (MAE). Here, a residual is defined as the radar precipitation accumulation minus the gauge precipitation accumulation. Results are provided for all radar-gauge pairs as well as for the subset where the gauge exceeds a threshold of 1.0, 10.0, and 20.0 mm day^{-1}. Note that representativeness errors can be significant when comparing radar and gauge accumulations (Kitchen and Blackall, 1992), especially for shorter durations, such as 1 h, and in case of larger differences in measurement volumes. The grid cell size of 4 km^2 is relatively large. Radars measure aloft, and rain gauges measure at the Earth's surface, but only over a small area. Hence, differences between radar and gauge accumulations can be partly attributed to representativeness errors.
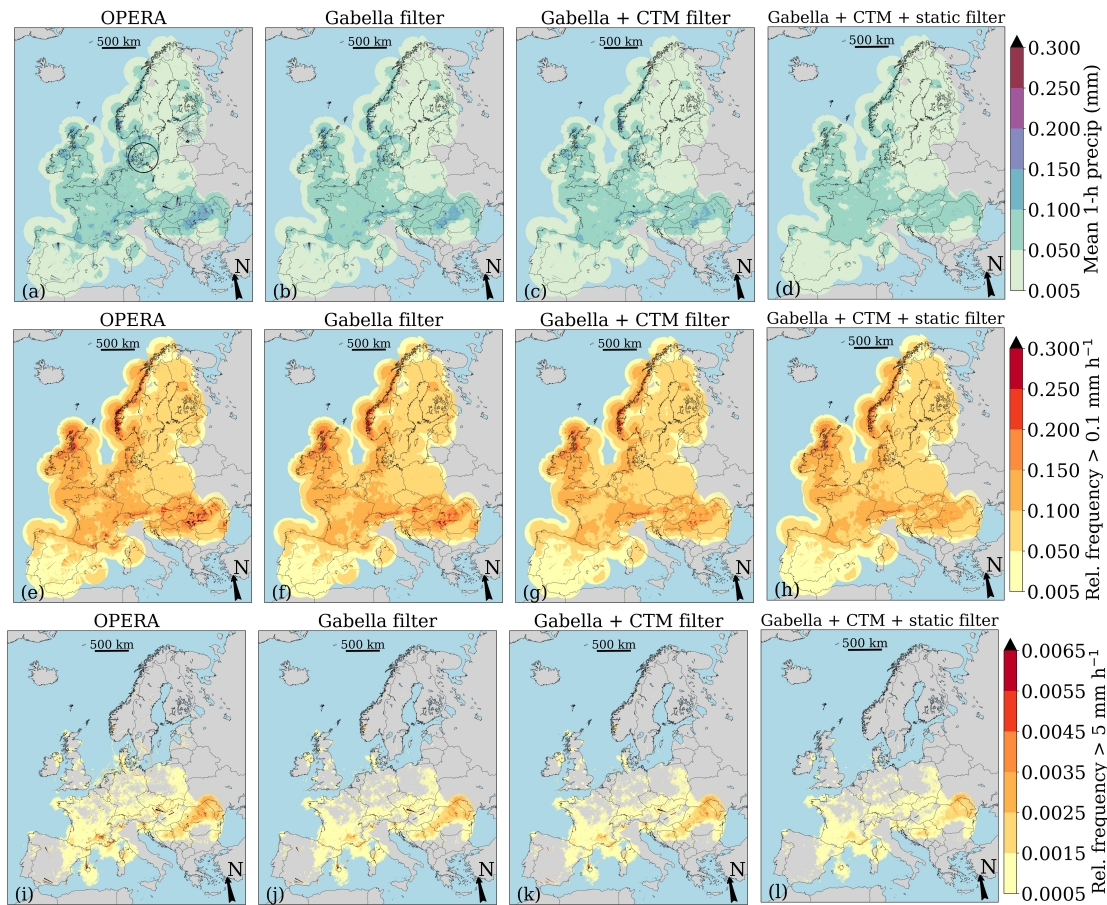
4   Results

The radar precipitation datasets are assessed by first systematically evaluating the influence of the clutter removal algorithms on QPE, followed by an evaluation of the performance of the EURADCLIM precipitation estimates. EURADCLIM's pan-European precipitation climatologies are shown and EURADCLIM's limitations are discussed. Finally, extreme precipitation events derived from EURADCLIM are presented.

4.1   Evaluation of clutter removal algorithms

Maps of mean hourly precipitation over the period 2013–2020 (Fig. 5a–b) show that the Gabella clutter filter removes and reduces many non-meteorological echoes, e.g., sea clutter at the North Sea, rings around Denmark, a radial pattern around Estonia, and spokes caused by interference over Slovakia. Also areas belonging to the highest precipitation class become smaller in Romania and southern France. Additional reductions are less pronounced when the cloud type mask is applied (Fig. 5b–c). A clear reduction in interferences in eastern Spain stands out and ~~again~~ areas falling in ~~the highest precipitation class generally become smaller~~ higher precipitation classes become smaller in Romania. The static clutter mask is effective in (strongly) reducing many of the remaining non-meteorological echoes ~~, but note~~ (Fig. 5c–d). When using a shorter color scale (not shown) it becomes visible that for some areas values may still be too high~~(Fig. 5c–d). And~~. And then the area in Europe known for the highest annual precipitation, the coastal area of Norway, also shows a strong reduction, which may point to unwarranted classification of non-meteorological echoes. This can be seen more clearly in Fig. A1c.

From the maps of relative frequency of 1-h precipitation exceeding 0.1 mm (Fig. 5e–f) and 5 mm (Fig. 5i–j) it can be concluded that the Gabella filter successfully removes non-meteorological echoes, especially sea clutter and suspicious noisy areas above land. The circles and radial patterns found for mean precipitation are not apparent, indicating that these do not occur frequently. For the 0.1 mm threshold, application of the cloud type mask clearly reduces the impact of ~~interference~~ interferences above Spain and some areas belonging to the highest precipitation ~~class become smaller~~ classes become smaller or disappear, especially in eastern Europe and south of the French Mediterranean coast. Apparent is that larger areas above ~~Germany and~~

Figure 5. Comparison between 1-h precipitation accumulations from four datasets to study the effect of non-meteorological echo removal algorithms over the period 2013–2020. Results are only shown for grid cells with a minimum availability of 83.3%. (a)–(d) Maps of mean hourly precipitation, and (e)–(l) maps of relative frequency of exceedance of 0.1 and 5 mm in an hour. These are obtained by dividing by the number of available values for each individual radar grid cell (i.e., not equal to "nodata" or not missing). This implies that periods with missing radar data are not taken into account and the number of intervals that is used will vary in space. Maps made with Natural Earth. Free vector and raster map data ©naturalearthdata.com.

~~Spain~~ France and Germany now belong to a lower frequency class, which could point to unwarranted classification of non-meteorological echoes. The cloud type mask hardly adds value in removing non-meteorological echoes for the 5 mm threshold, apart from reducing the frequency of the impact of interferences (Fig. 5j–k). The static clutter mask successfully removes non-meteorological echoes for the 0.1 mm threshold (Fig. 5g–h) in eastern Europe and for the 5 mm threshold (Fig. 5k–l) ~~remaining interferences are successfully removed~~ the frequency of remaining interferences is successfully decreased over all of Europe. The fraction in mean rainfall and the fraction in relative frequencies of these datasets, which have undergone additional clutter removal, with respect to the OPERA dataset are presented in Appendix A1,

14

Conclusion is that the algorithms remove many and also severe non-meteorological echoes. To evaluate the unwarranted removal of precipitation echoes, daily radar accumulations are compared to daily gauge accumulations in Table 1. This independent evaluation for different threshold values, shows that differences in the value of MAE between the four datasets are small, the value of CV usually decreases and the value of ρ usually increases after each additional processing step. The

315   strongest improvement is found for the Gabella clutter filter and the static clutter filter. The relative bias in the mean daily precipitation becomes much more negative, though. The non-meteorological echoes may have compensated for the large underestimation that is typical for mid-to-high latitude radar-only precipitation estimation (Overeem et al., 2009b). Because of the general improvement for other statistical metrics, it is concluded that the clutter removal algorithms are effective and remove few precipitation echoes. Concluding, the radar dataset that will be used for merging with rain gauge data has improved

320   considerably over the dataset where no additional filtering is applied, in terms of ~~the correlation~~ ρ and CV.

As a final check of the effectiveness of the clutter filter, daily radar accumulations are selected when the daily gauge accumulation is 0 mm. This results in average daily accumulations of 0.5 mm when no filtering is applied and this decreases to 0.3 mm for the Gabella filter and to 0.2 mm when also the cloud type mask is applied. This confirms the effectiveness of the algorithms to further remove non-meteorological echoes. It remains 0.2 mm, though, when also the static clutter filter is applied. This

325   ~~confirms the effectiveness of the algorithms to further remove non-meteorological echoes.~~ is likely a result of the static clutter mask being only applied to a small part of the OPERA domain (see, e.g., Fig. 4h), which contains a small minority of the rain gauges. As a consequence, positive effects are small when comparing to rain gauges from the entire OPERA domain. Moreover, in contrast to the other clutter filtering algorithms, values are not removed but interpolated from surrounding values. Hence, no clear improvement at the location of the gauges is found for the static clutter mask.

330   **4.2   Evaluation of EURADCLIM**

In Table 1, a dependent verification of daily radar precipitation accumulations against rain gauges is performed to quantify the influence of the adjustment employing gauge data (i.e., with respect to the "Gabella + CTM + static filter" dataset). Results are presented for all values and for those where gauges exceed specific thresholds. Note that all selected values are used to compute the statistical metrics. A number of conclusions can be drawn from Table 1: 1) the severe average underestimation of

335   precipitation of $\sim 45\%$ turns into an overestimation of $\sim 11\%$ for EURADCLIM; 2) for daily gauge precipitation above 1 mm the relative bias is near zero; 3) the large underestimation for very heavy precipitation days (over 20 mm per day) is reduced from $\sim 65\%$ to about $\sim 10\%$; 4) the ~~values~~ value for the correlation coefficient strongly increases from 0.59 to 0.89 based on all precipitation events; 5) the values for CV strongly decrease with a factor between 1.3 and 1.7; 5) the values for MAE ~~decreases~~ decrease to values that are between 1.7 and 3.2 times smaller. The scatter density plots provide a more complete overview of

340   the improvement and show the much better alignment along the 1:1 line compared to the unadjusted dataset for daily gauge precipitation above 1 mm (Fig. 6a–b). The quality of daily precipitation accumulations is higher in summer (June, July, August; Fig. 6d) than in winter (December, January, February; Fig. 6~~c~~dc). Although differences in the values of statistical metrics are relatively small, the spread in the scatter density plot for summer is clearly lower than in winter. Apparent are the (near) zero precipitation values for a wide range of rain gauge values. 54% of all data points for which the daily gauge accumulation is

15

Table 1. Evaluation of radar daily precipitation accumulations against the ECA&D rain gauge network over the period 2013–2020 at their default measurement interval for all radar-gauge pairs and for those above a threshold value. The mean daily precipitation and the threshold value are based on the gauge data. ~~Relative bias, Pearson correlation coefficient, mean absolute error and coefficient of variation are provided, respectively.~~

| Threshold value (mm)	Mean daily precipitation	Rel. bias (%)	~~Correlation~~ ρ	MAE (mm)	CV	n
No filtering:						
	2.41	-25.3	0.11	1.85	8.40	18946028
1.0	7.41	-42.7	0.17	4.50	2.44	5970041
10.0	19.52	-55.3	0.22	11.88	0.85	1299677
20.0	32.05	-61.4	0.25	20.69	0.56	401277
Gabella clutter filter:						
	2.41	-38.8	0.19	1.61	5.06	18930248
1.0	7.41	-47.9	0.42	4.34	1.15	5964987
10.0	19.52	-57.6	0.35	11.91	0.63	1299043
20.0	32.05	-63.0	0.29	20.86	0.50	401049
Gabella + CTM clutter filter:						
	2.41	-42.0	0.21	1.58	4.47	18936402
1.0	7.41	-49.5	0.45	4.40	1.11	5967504
10.0	19.52	-58.5	0.35	12.06	0.62	1299285
20.0	32.05	-63.7	0.29	21.07	0.50	401091
Gabella + CTM + static clutter filter:						
	2.41	-44.9	0.59	1.55	2.01	18930115
1.0	7.41	-51.0	0.59	4.39	0.96	5964938
10.0	19.52	-59.9	0.41	12.16	0.57	1299042
20.0	32.05	-65.2	0.32	21.30	0.47	401049
EURADCLIM:						
	2.41	10.8	0.89	0.89	1.18	18929782
1.0	7.41	-0.1	0.88	1.88	0.58	5964696
10.0	19.52	-7.1	0.78	4.03	0.42	1298998
20.0	32.05	-10.2	0.73	6.75	0.36	401047

345 above 20 mm and the corresponding EURADCLIM radar accumulation is below 1 (Fig. 6b), are located in Italy, and are likely related to beam blockage or overshooting.

For hourly precipitation, both an independent verification via leave-one-out-statistics and a dependent verification are performed. The scatter density plots show the radar-gauge pairs for 1-h gauge precipitation larger than 0.25 mm (Fig. 6e–g). The remaining underestimation becomes small and the value for the coefficient of determination (ρ^2) increases with respect to the unadjusted radar dataset, especially for the dependent verification. For EURADCLIM, the value for CV increases for the independent verification. The second lowest count class becomes rather wide above the 1:1 line. For the dependent verification the scatter density plot is much better aligned to the 1:1 line and the value for CV becomes much lower compared to the unadjusted dataset. Conclusion is that the quality of the EURADCLIM dataset is good and much better than the dataset that has undergone the clutter filtering but no gauge adjustment. Note that the verification via LOOS is not entirely independent, because the 1-h and 24-h radar accumulations have been employed to disaggregate the daily gauge accumulations to hourly accumulations.

Next, a spatial verification per rain gauge location is performed for the radar dataset before gauge adjustment and for EURADCLIM, again for an independent (LOOS) and a dependent verification (Fig. 7). The quality of the radar composite for the unadjusted radar dataset displays quite some variability and there seems some connection with areas further away from the nearest radar (Fig. 2c). Also different environmental conditions, e.g., ~~beam-blockage~~ beam blockage due to mountainous terrain, can play a role. The values for ρ, CV and relative bias in the mean strongly improve for the EURADCLIM dataset (dependent verification; Fig. 7c,f,i) with respect to the unadjusted radar dataset. In addition, the spatial variability in performance becomes much smaller. However, for the independent verification for regions with low gauge network densities, the value for ρ sometimes decreases, the value for CV often increases and the underestimation becomes either less severe or turns into large overestimation (Fig. 7b,e,h) with respect to the unadjusted radar dataset. Note that the dependent verification shows the actual performance of EURADCLIM at those locations, and that the independent verification is meant to give an impression of the quality between those locations. In reality, results are expected to be better for EURADCLIM than found for ~~the~~ this independent verification, because the distance to the nearest gauge will be much shorter. ~~After all, the gauges that are left out for LOOS have been used in the final EURADCLIMdataset.~~ For the LOOS results, the gauge-adjustment has been rerun for each gauge location while using all available radar-gauge pairs except the one at the considered gauge location. Whereas for EURADCLIM, all available radar-gauge pairs are used.

Finally, for some gauge locations large differences are found. For instance, for two nearby stations in Poland a large overestimation and a large underestimation are found. Also the values for CV are high. This may point to erroneous rain gauge data. For other regions, radar ~~beam-blockage~~ beam blockage could play a role.
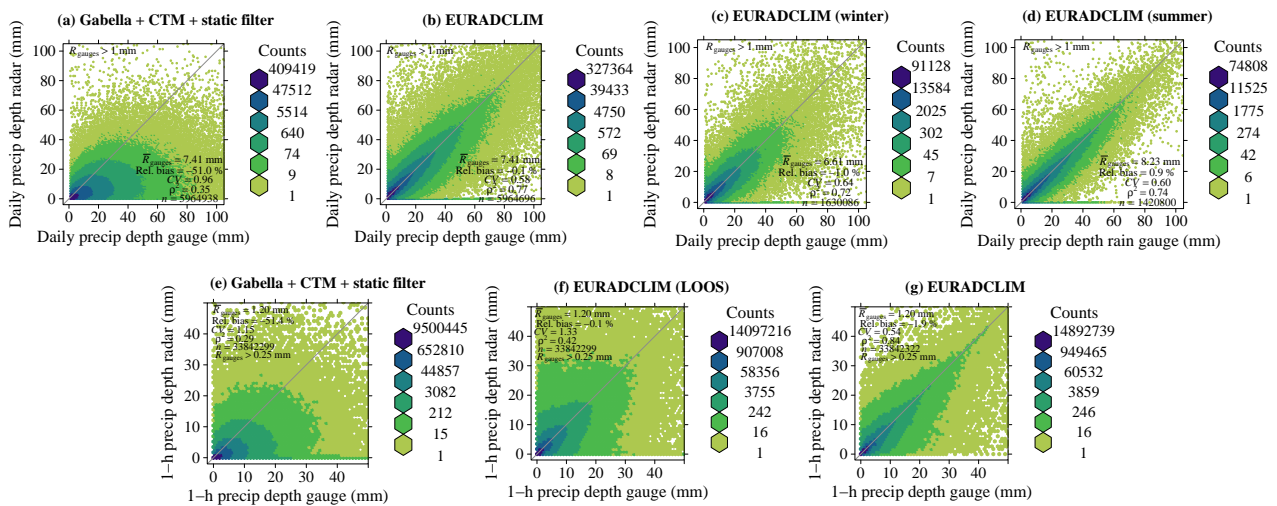
Figure 6. Scatter density plots of (a)–(d) daily and (e)–(g) 1-h radar precipitation accumulations against rain gauges over the period 2013–2020. For daily accumulations the gauge accumulations at their default measurement interval are employed, whereas for 1-h accumulations the disaggregated clock-hourly gauge precipitation accumulations are employed. Results are shown for the unadjusted dataset that has undergone all clutter filtering steps and for the gauge-adjusted EURADCLIM dataset. For EURADCLIM, independent verification is done via leave-one-out-statistics (LOOS), when ~~indication~~indicated. Otherwise, the verification is dependent.
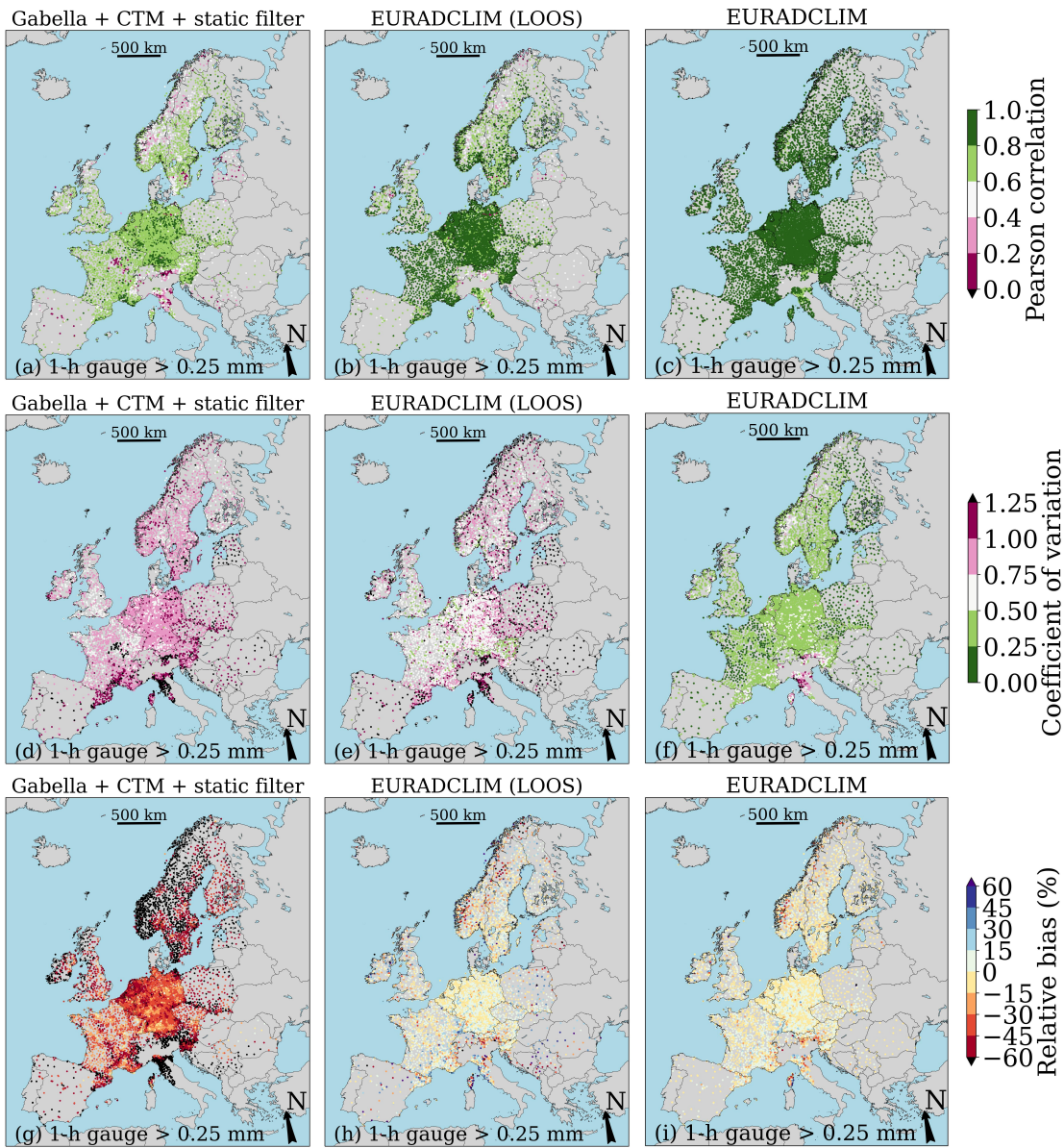
Figure 7. Spatial verification of 1-h precipitation accumulations against the disaggregated clock-hourly gauge precipitation accumulations over the period 2013–2020. (a, d, g) For the unadjusted radar dataset that has undergone all clutter filtering steps. Results from the gauge-adjusted EURADCLIM dataset are shown for (b, e, h) an independent verification employing leave-one-out-statistics (LOOS) and for (c, f, i) a dependent verification. Maps made with Natural Earth. Free vector and raster map data ©naturalearthdata.com.

4.3 EURADCLIM radar precipitation climatologies and its limitations

375 Despite the efforts by NMHS and OPERA to remove non-meteorological echoes, and the three additional clutter removal algorithms employed to derive EURADCLIM, still non-meteorological echoes can be persistent for some areas (Fig. 5h). Two cases with strong artefacts are shown in Fig. 8 for the original OPERA surface rain rates. For the first case, the entire radar domain of a Spanish radar has very high rates, which seems to be caused by a constant signal source that lasted the first 7 hours of 29 April 2018 (Fig. 8a). Since this occurs over an entire radar domain, the algorithms can only partly remove and reduce these

380 ~~non-meteorological echoes~~ echoes caused by failures of radar processing (unless entirely cloud-free or only semi-transparent clouds). This is much reduced by the gauge adjustment, although still 24-h precipitation accumulations of more than 50 mm are found in EURADCLIM (Fig. 8b). For the second case (Fig. 8c) with strong artefacts from a French radar, the 1-h precipitation accumulations are substantially reduced by the EURADCLIM algorithms (Fig. 8d). Again, this reduction is primarily caused by the gauge adjustment. Still, Fig. 8b,d indicates that EURADCLIM sometimes contains substantial artefacts.

385 Now the quality of EURADCLIM has been quantified, precipitation climatologies are derived to show its potential (Fig. 9). A map of mean hourly precipitation over the period 2013–2020 is shown in Fig. 9a. There are still some signatures of ~~beam-blockage,~~ beam blockage (e.g., Austria, Italy, northwestern Spain in Fig. 9a), probably caused by obstacles near radar sites, and of non-meteorological echoes, such as ~~interference.~~ interferences (e.g., Bosnia and Herzegovina, eastern Spain in Fig 9a,f,g). The highest precipitation values are found in the coastal areas of Norway and in some mountainous areas (e.g., the

390 Alps, Bosnia and Herzegovina, Croatia, Ireland, Norway, Scotland, and Wales). The seasonality of mean hourly precipitation is visualized in Fig. 9b–e. In Western Europe, precipitation is highest in autumn and winter. The Mediterranean areas are typically dry in winter and summer and relatively wet in spring and autumn. Apparent is the high seasonal precipitation in the Alps in summer. Relative frequencies of exceeding 0.1 mm are displayed in Fig. 9f, revealing that 1-h precipitation is most frequent in Denmark, Ireland, large parts of the United Kingdom, parts of Norway, and a patchy band from France to Switzerland and

395 Germany to parts of Eastern Europe. The southern part of Spain has the lowest frequency of 1-h precipitation exceeding 0.1 mm. The relative frequency of exceeding 5 mm (Fig. 9g) shows that more extreme precipitation occurs most often in parts of southern Europe and parts of Ireland and the United Kingdom. It is difficult to tell to what extent non-meteorological echoes play a role here. For instance, some of the localized areas with high frequencies of exceeding 5 mm may be related to obstacles near radar sites. This becomes even more apparent for downpours of more than 25 mm in 1 hour (Fig. 9h), where large areas

400 are found with at least 13 occurrences in 8 years, sometimes present over a large part of a radar domain. These large values at the edge of radar coverage are suspicious, especially when no nearby rain gauges are available, such as east of the island of Corsica (France). When comparing the mean daily precipitation and relative frequencies of exceeding 0.1 mm and 5 mm to those from the unadjusted radar data in Fig. 5, it is clear that these strongly increase after the gauge adjustment. This can also lead to non-meteorological echoes becoming more pronounced (e.g., interferences in eastern Spain in Fig. 9f compared to Fig.

405 5h).

~~Outliers, such as presented in Fig. 8 and visible in the frequency of downpours (Fig. 9h), limit the applicability of EURADCLIM at the grid cell scale, especially for use in extreme value modelling (e.g. Frederick et al., 1977; Durrans et al., 2002; Allen and DeGaetano,~~
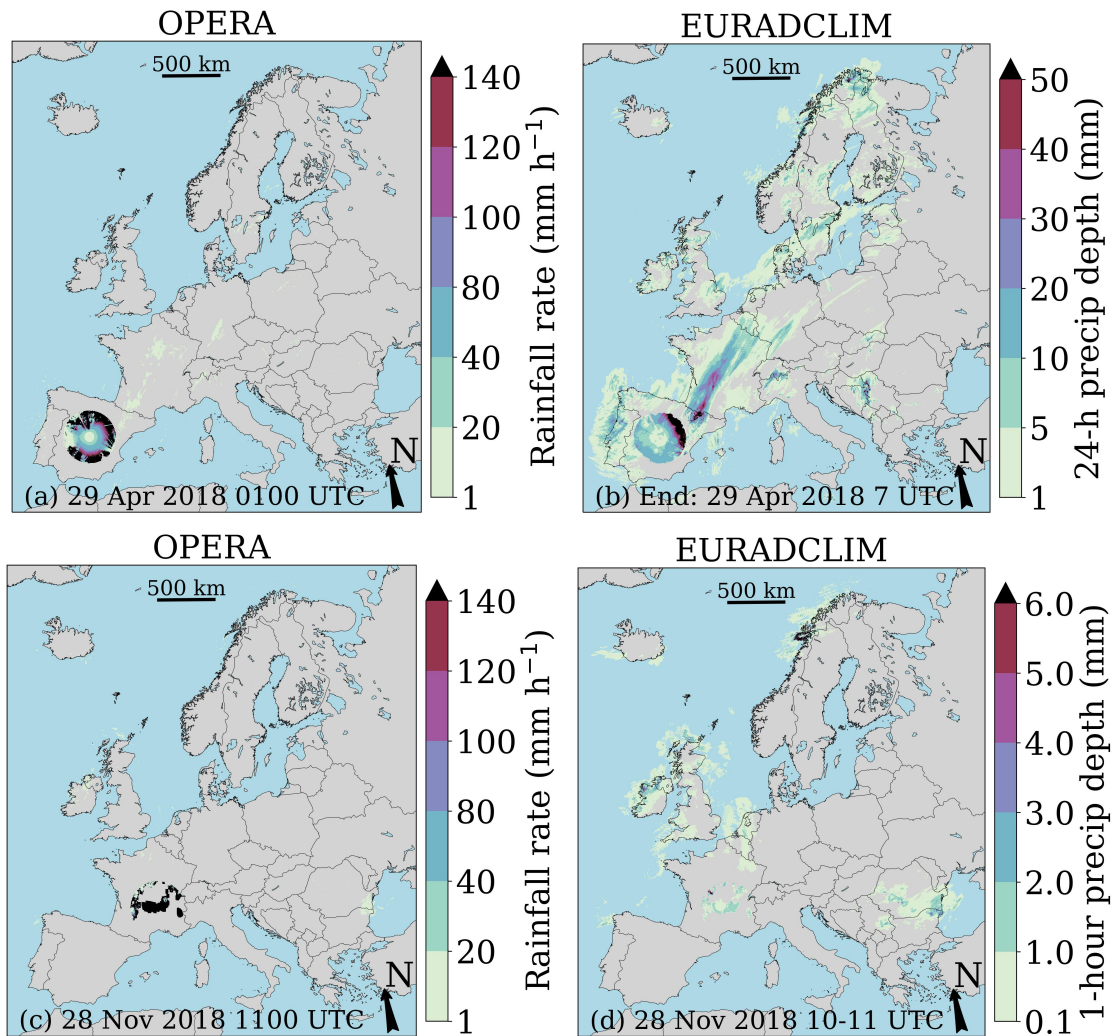
Figure 8. Illustration of remaining non-meteorological echoes in radar data for the original instantaneous OPERA rain rates and the corresponding 24-h or 1-h precipitation accumulations from EURADCLIM. (a)–(b) ~~"Extreme~~ ~~precipitation"~~ values in central Spain on 29 April 2018 0100 UTC (rain rate) and from 28 April 2018 0700 UTC – 29 April 2018 0700 UTC (24-h precipitation accumulation). The gauge adjustment helps to lower the accumulations in EURADCLIM. (c–d) An extreme case with more than 500 mm h^{-1} over large parts of a French radar domain on 28 November 2018 for 1100 UTC. Clutter removal algorithms hardly help, but the gauge adjustment substantially reduces the 1-h precipitation accumulations from EURADCLIM from 1000-1100 UTC. Maps made with Natural Earth. Free vector and raster map data ©naturalearthdata.com.

~~. One way to deal with this is to apply an algorithm that does not take into account entire composites that have severe artefacts over larger areas. These could be automatically identified by radar-gauge comparison, possibly followed by a visual inspection~~
410 ~~and selection. Another approach would be to set grid cells above a certain threshold to a lower (e.g., interpolated) value. Or~~
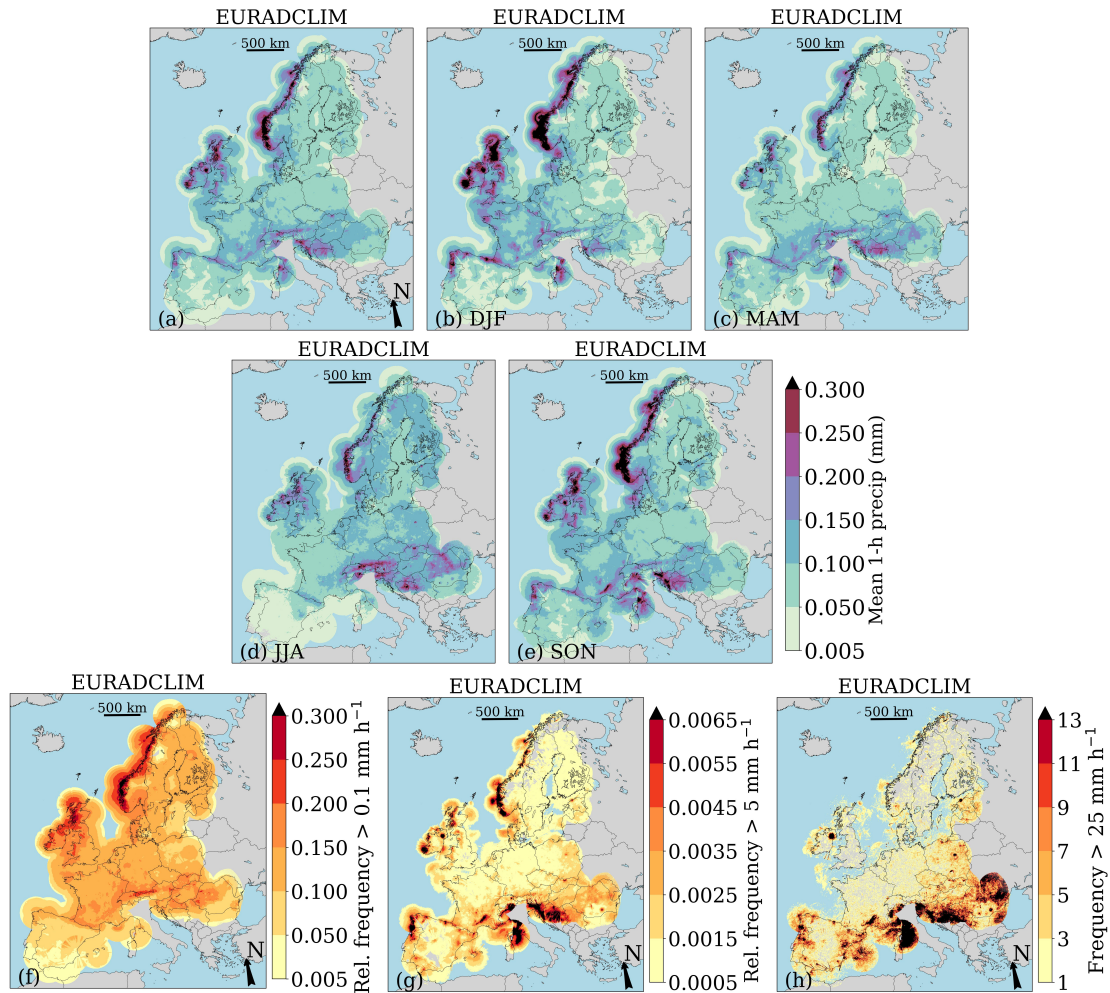
Figure 9. (a)–(e) Maps of mean hourly precipitation over the entire period and per season over the period 2013–2020 (winter: December, January, February; spring: March, April, May; summer: June, July, August; autumn: September, October, November). (f)–(g) Relative frequency of exceedance of 0.1 and 5 mm in an hour over the period 2013–2020, respectively. (h) Frequency of exceedance of 25 mm in an hour, a downpour, over the period 2013–2020. Relative frequencies of exceedance ((f)–(g)) are obtained by dividing by the number of available values for each individual radar grid cell (i.e., not equal to "nodata" or not missing). This implies that periods with missing radar data are not taken into account and the number of intervals that is used will vary in space. For (a)–(g) results are only shown for grid cells with a minimum availability of 83.3%. Maps made with Natural Earth. Free vector and raster map data ©naturalearthdata.com.

always discard such a grid cell if it experienced such a high value at least once during the period 2013–2020. A drawback of this approach is that such a threshold is a bit arbitrary and that it influences statistics of extreme precipitation. A more sophisticated approach would be to remove more non-meteorological echoes by applying a satellite cloud mask that employs cloud optical thickness, i.e., also in case of thicker non-precipitating clouds.Finally, in the future, MSG will be replaced by Meteosat Third

415 ~~Generation that allows for a more local correction due to higher spatial and temporal resolution, provided that parallax effects are accounted for.~~

An additional comparison is presented in Appendix A2, where the eight EURADCLIM annual precipitation accumulations are compared to those from the gridded rain gauge dataset E-OBS. Generally, precipitation patterns agree, but many local differences can be found. At far range from radars and rain gauges, a decrease in annual precipitation is found (e.g., above
420 sea). Artefacts in radar accumulations, especially spokes caused by interference, result in overestimation in some regions. The E-OBS data are based on all days, whereas EURADCLIM has some missing data, especially the first ∼three weeks of 2013 do not have data. Note that E-OBS has a grid of 0.1°, which is much coarser than the 2-km radar grid. More importantly, the underlying gauge network density can be sparse, whereas EURADCLIM provides full coverage. Hence, differences between EURADCLIM and E-OBS are expected and Appendix A2 is meant as an illustration and sanity check for both datasets.

425 ## 4.4 EURADCLIM extreme precipitation events

Figure 10 shows EURADCLIM's precipitation estimates for three ~~precipitation events~~(more) extreme precipitation events meant to illustrate EURADCLIM's potential: a wide-spread event across Europe showing the associated precipitation pattern of an extratropical cyclone with locally more than 60 mm in 24 hours (Fig. 10a). An extreme event in eastern Europe with at least 120 mm in 24 hours (Fig. 10b). And a very extreme event in southern France with at least 350 mm locally in 24 hours, of
430 which at least 80 mm in the last hour (Fig. 10c–d). These events illustrate that EURADCLIM can capture extreme precipitation events across Europe, which can especially be valuable for regions where climatological radar precipitation datasets do not exist or are not open, and where the affected area spans multiple countries.

5 Conclusions

We presented a climatological gauge-adjusted radar dataset of 1-h and 24-h precipitation accumulations, EURADCLIM, cov-
435 ering a large part of Europe over the period 2013–2020. Clearly, EURADCLIM will not outperform national (climatological) radar precipitation datasets (e.g. Overeem et al., 2009b; Goudenhoofdt and Delobbe, 2016; Winterrath et al., 2018; Saltikoff et al., 2019a; KNMI, 2022). The spatiotemporal resolution of (the underlying) composites will often be higher, e.g., 5 min or 10 min instead of 15 min and 1 km^2 instead of 4 km^2. In addition, they may have undergone additional processing (e.g., based on 3D radar data) or may use more rain gauge data. These are expected to increase the accuracy of QPE with respect to
440 EURADCLIM. However, such national datasets often do not exist or are not freely available for research or other purposes. Moreover, EURADCLIM allows users to use a common dataset for a large part of Europe, instead of using different datasets from multiple countries. EURADCLIM will also benefit from possible future improvements in the OPERA surface rain rate product.

Apart from the evaluation of EURADCLIM, the performance of the OPERA precipitation product and three clutter removal
445 algorithms were evaluated over an 8-year period. Some of the processing steps could also be applied in (near) real-time and would help to further improve the OPERA precipitation products. As is shown, the Gabella clutter filter would clearly decrease
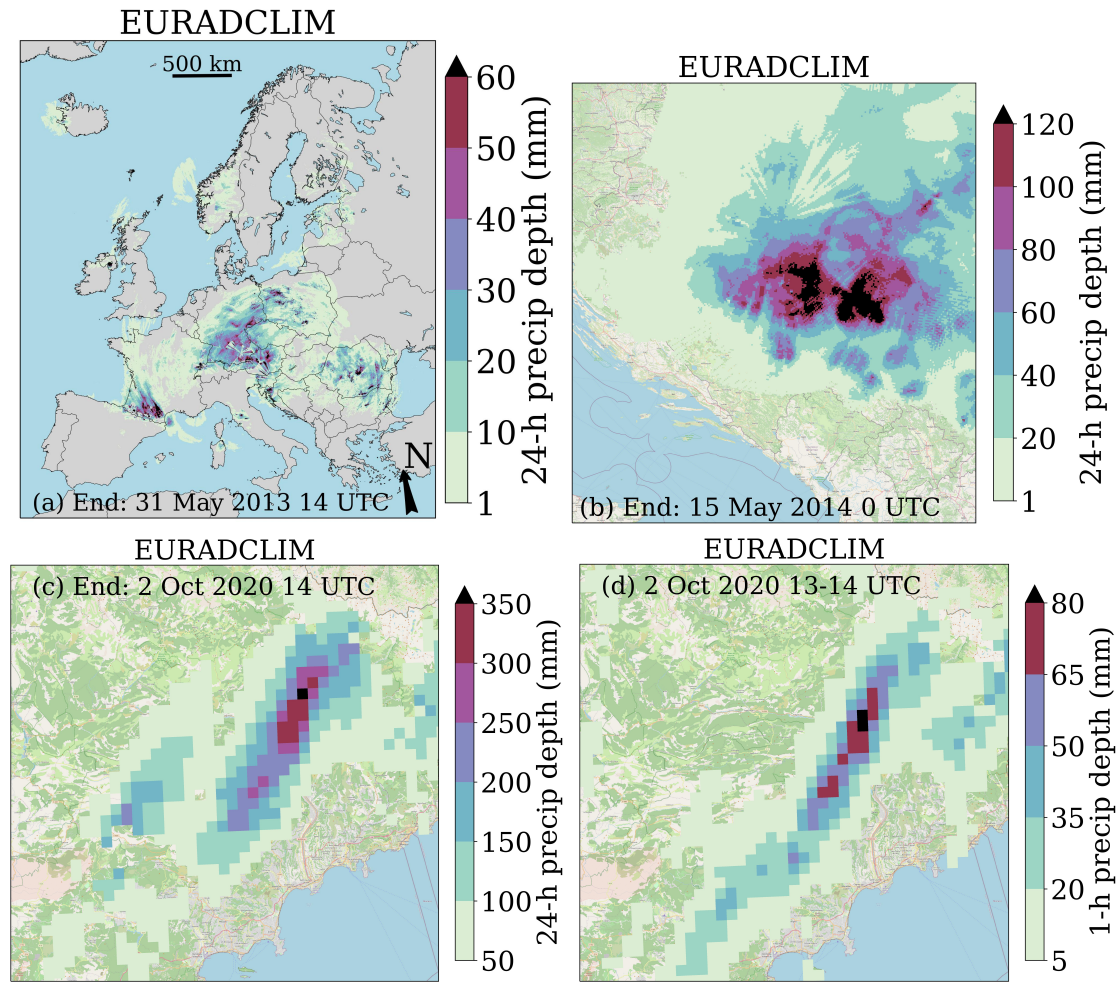
Figure 10. Three precipitation events that led to flooding. (a) A widespread event over Europe from 30 May 2013 1400 UTC – 31 May 2013 1400 UTC (24-h precipitation accumulation), which is also presented as Supplement (Movie S1). (b) An event in eastern Europe from 14 May 2014 0000 UTC – 15 May 2014 0000 UTC (~~1-h~~ 24-h precipitation accumulation), and (c)–(d) a very extreme event north of Nice, southern France from 1 October 2020 1400 UTC – 2 October 2020 1400 UTC (24-h precipitation accumulation) and its last hour (1-h precipitation accumulation). (a) Map made with Natural Earth. Free vector and raster map data ©naturalearthdata.com. (b)–(d) map data ©OpenStreetMap contributors 2022. Distributed under the Open Data Commons Open Database License (ODbL) v1.0.

non-meteorological echoes in the OPERA product and would be directly applicable. OPERA already uses a satellite cloud mask. The static clutter mask could be applied if the annual precipitation accumulations from the previous year would be used. When sub-daily near real-time gauge accumulations would become available, this would pave the way for merging with OPERA radar accumulations in near real-time, e.g., by merging data from the last clock-hour. We think this would be a useful improvement of the product developed by Park et al. (2019). The correction for motion of the precipitation field from Park

450

et al. (2019) could be a valuable addition to EURADCLIM. Moreover, in line with Park et al. (2019), the temporal resolution of EURADCLIM could be increased to 15 min. Finally, the period of the evaluation by Park et al. (2019) of OPERA-based QPE as a function of time, could be extended, and this daily monitoring could also be applied to EURADCLIM.

455   This first version of EURADCLIM should be seen as a starting point. Despite the different algorithms to remove non-meteorological echoes applied by NMHS, OPERA and in EURADCLIM, these echoes do still pose a problem. We claim that precipitation climatologies derived from EURADCLIM have a reasonable accuracy and that extreme events can be captured at a much higher spatiotemporal resolution, but that EURADCLIM is not directly suited yet for extreme value modelling at the grid cell scale, which requires records of the most extreme events, such as annual maxima. EURADCLIM may already be

460 suitable for extreme value modelling in case of longer durations or larger area sizes than the grid cell scale, such as larger hydrological catchments. Then non-meteorological echoes may average out. We also recommend to compare the EURADCLIM precipitation accumulations to those from national radar datasets, specifically to assess the performance of EURADCLIM to capture extreme precipitation.

    Outliers, such as presented in Fig. 8 and visible in the frequency of downpours (Fig. 9h), limit the applicability of EURADCLIM

465 at the grid cell scale, especially for use in extreme value modelling (e.g. Frederick et al., 1977; Durrans et al., 2002; Allen and DeGaetano, . Here, we provide some recommendations to end users to deal with these outliers:

- One way to deal with this is to apply an algorithm that does not take into account entire composites that have severe artefacts over larger areas. These could be automatically identified by radar-gauge comparison, possibly followed by a visual inspection and selection. For instance, the number of grid cells with a large ratio between gauge and radar
470   accumulations could be counted. If the total count exceeds a threshold, the interval can be labelled as suspicious.

- Another approach would be to set grid cells above a certain threshold to a lower (e.g., interpolated) value. Or always discard such a grid cell if it experienced such a high value at least once during the period 2013–2020. A drawback of this approach is that such a threshold is a bit arbitrary and that it influences statistics of extreme precipitation. For example, grid cells with annual precipitation clearly above that of local climatological gauge records could be discarded, as well
475   as grid cells with unlikely high values for 24-h precipitation.

    QPE could be further improved, especially in areas with sparse rain gauge network density or far away from weather radars. Some regions are far away from rain gauges, making the merging algorithm less effective. In some cases no merging is even carried out because of the long distance to the nearest rain gauge (e.g., Iceland, Malta). To improve the quality of EURADCLIM, but also the OPERA near real-time precipitation products, we provide the following main recommendations

480 for NMHS, the OPERA program and EURADCLIM:

- Start with the volumetric radar data and apply algorithms (Goudenhoofdt and Delobbe, 2016) such as fuzzy logic clutter removal (Berenguer et al., 2006; Gourley et al., 2007; Crisologo et al., 2014; Krause, 2016; Overeem et al., 2020), attenuation correction (Carey et al., 2000; Testud et al., 2000; Vulpiani et al., 2012; Al-Sakka et al., 2013; Jacobi and Heistermann, 2016; Overeem et al., 2021) and vertical profile of reflectivity correction (Hazenberg et al., 2013). Es-
485   pecially the use of polarimetric variables would add value, also in the conversion to rain rates. Moreover, differences

between weather radars, e.g., polarimetric or not, and climate would require careful local analyses and optimization of parameters (e.g., fuzzy logic settings, precipitation retrieval relations for rain/snow).

– Obtain gauge data from more locations and update the rain gauge records that overlap with the (extended) EURADCLIM time span. Additional high quality data might come from, e.g., NMHS, water and river authorities, and other data-holding institutes. Instead of using only daily data, ideally also clock-hourly data would become available, which would avoid possible errors introduced by disaggregating daily precipitation. This is desirable given the often large spatial and temporal variability in precipitation and in sources of error in radar QPE.

– Specifically, third party data could be employed after appropriate quality control (and retrieval) algorithms have been applied. This also requires efforts from NMHS to bring these from research to operations (?)(Garcia-Marti et al., 2023) . Examples of such third-party data sources are rain gauge data from personal weather stations (PWS) connected to the internet (De Vos et al., 2019; Graf et al., 2021) and commercial microwave link (CML) data (Messer et al., 2006; Leijnse et al., 2007; Overeem et al., 2016; Graf et al., 2020, 2021). The merging of these kind of datasets with radar data is studied in the COST action OPENSENSE OpenSense (https://opensenseaction.eu/). These data sources could potentially be available in (near) real-time and would give a vast increase in the density of surface precipitation estimates. However, the increase over time of the number of available third party data, challenges the aim of EURADCLIM to provide a climatic perspective on hourly rainfall.

– Develop a radar-gauge merging algorithm that takes into account the local rain gauge network density. For the current method, the local mean-field bias adjustment followed by a spatial adjustment could then be replaced by a spatial adjustment where the value of the short range parameter varies seamlessly in space as a function of network density. In addition, the value of the short range parameter should be based on the local precipitation climatology instead on the precipitation climatology from the Netherlands. Also other adjustment methods could be evaluated (Goudenhoofdt and Delobbe, 2009).

– Add uncertainty information to radar and gauge data and use this in the radar-gauge merging. For instance, by using the OPERA quality index and additional information on the radar quality and the rain gauge network density. Alternatively, it could be studied whether a meaningful relationship can be established between the quality of EURADCLIM and the distance to the nearest gauge or radar. Then maps with distance to the nearest gauge or radar (Fig. 2c–d) could guide the user to judge the suitability of using a certain grid cell or region of EURADCLIM for a given application. Ideally, such quality maps would be computed for each 1-h interval, taking into account the gauges actually used in the merging and the radar coverage and quality for that time interval. To facilitate this, we recommend to add the actual radar coordinates for each individual time interval to the OPERA products.

– A more sophisticated approach would be to remove more non-meteorological echoes by applying a satellite cloud mask that employs cloud optical thickness, i.e., also in case of thicker non-precipitating clouds.

- Finally, in the future, MSG will be replaced by Meteosat Third Generation that allows for a more local correction due to higher spatial and temporal resolution, provided that parallax effects are accounted for.

520   EURADCLIM's strategic value encompasses:

- Much better reference for validation of weather prediction model output (e.g., HARMONIE/ECMWF) (Van der Plas et al., 2017), Regional Climate Model simulations (Berg et al., 2019), satellite precipitation products (Skofronick-Jackson et al., 2018; Sun et al., 2018), and opportunistic sensing data (e.g., CML and PWS), which allows for improving their quality control or retrieval algorithms.

525
- Better monitoring of (trends in) precipitation extremes and their spatial extent, except for the most extreme events at the grid cell scale, such as annual maxima, due to remaining non-meteorological echoes. This facilitates better understanding of the drivers behind such events (e.g., the relation to dew point temperature, atmospheric circulation, diurnal cycle, clustering of showers) and climate attribution (Lochbihler et al., 2017; Lengfeld et al., 2019). Deriving a catalogue of extreme precipitation events becomes possible, as is done for Germany by Lengfeld et al. (2021). This is all highly

530   relevant for anticipating future extremes in a changing climate.

- Better evaluation of extreme precipitation events and their impact (e.g., landslides, flooding). Specifically, use as input for hydrological models in order to improve these models, especially for flash flood forecasting.

We expect to rerun EURADCLIM once a year over the entire period, using all available ECA&D rain gauge data, and extend it with one year of data. This will result in a new version of this dataset. Hence, we invite NMHS or other institutes

535   to make all their rain gauge data available to ECA&D. We encourage to start using EURADCLIM and discover its value and shortcomings for a variety of applications, and we appreciate any feedback on this. It is expected that EURADCLIM will be of use to various (scientific) domains and applications and that future collaborations and funding will lead to improved next versions of EURADCLIM.

6   Code availability

540   The following tools, written in programming language Python (version 3), are publicly available at the GitHub repository EURADCLIM-tools (https://github.com/overeem11/EURADCLIM-tools) (Overeem, 2022), to process OPERA-based radar precipitation files: a script to accumulate data, a script to perform climatological analyses (e.g., to compute the mean and the relative frequency of exceedance), two scripts to visualize precipitation, one of them with an OpenStreetMap or Google Maps as background. This can help end users to visualize precipitation maps and to further explore and analyze the EURADCLIM

545   dataset.

27

7 Data availability

The EURADCLIM 1-h and 24-h precipitation datasets are available from the KNMI Data Platform. The dataset of 1-h precipitation is available at https://doi.org/10.21944/7ypj-wn68 (Overeem et al., 2022a). The dataset of 24-h precipitation is available at https://doi.org/10.21944/1a54-gg96 (Overeem et al., 2022b). For each year a zip file is provided. The data are in UTC, where
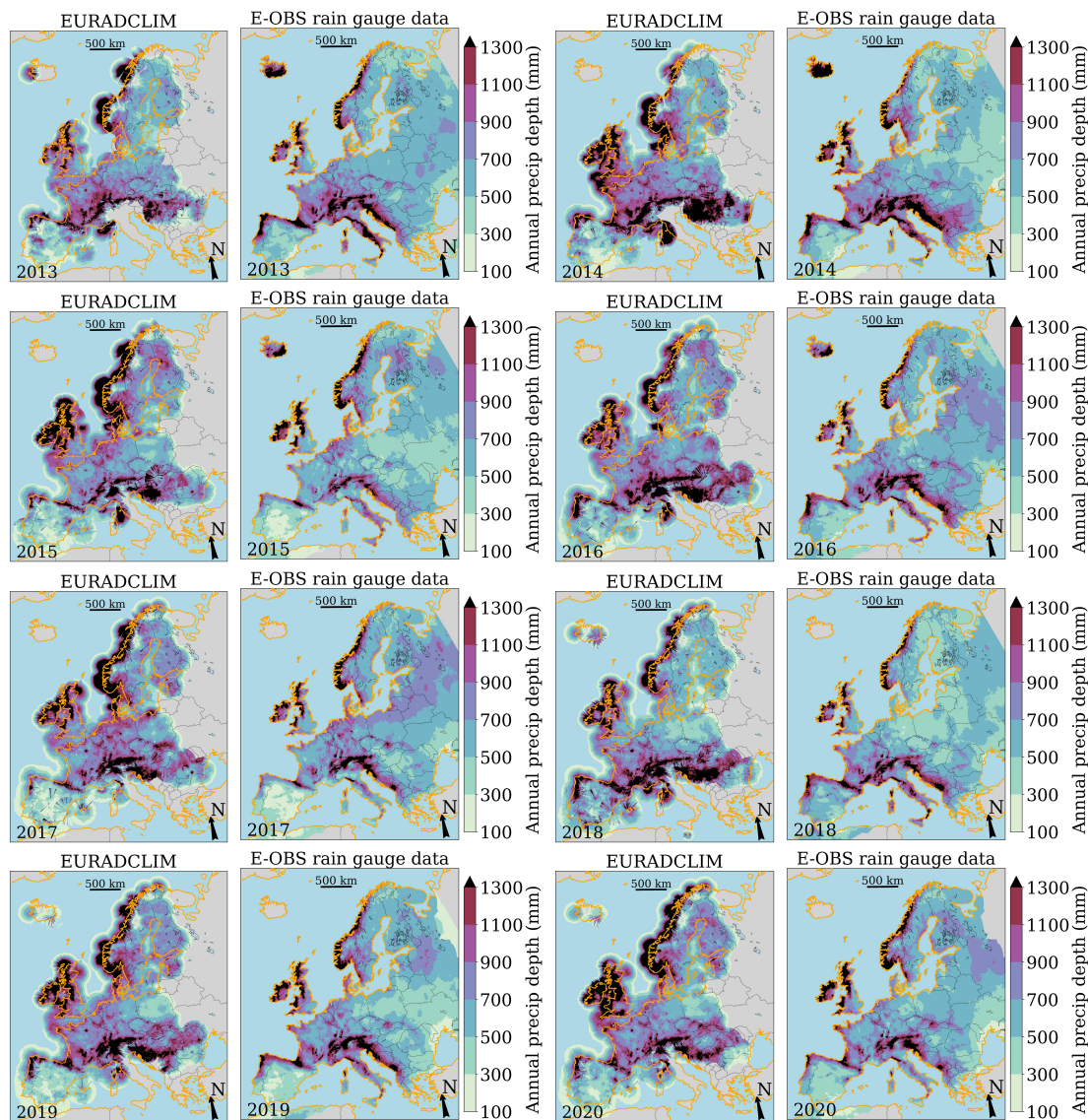550   the time in the unzipped filenames is the end time of observation in UTC.

Video supplement. The supplemental video visualizes a widespread precipitation event on 30 and 31 May 2013 over Europe that led to flooding. Supplement (Movie S1).
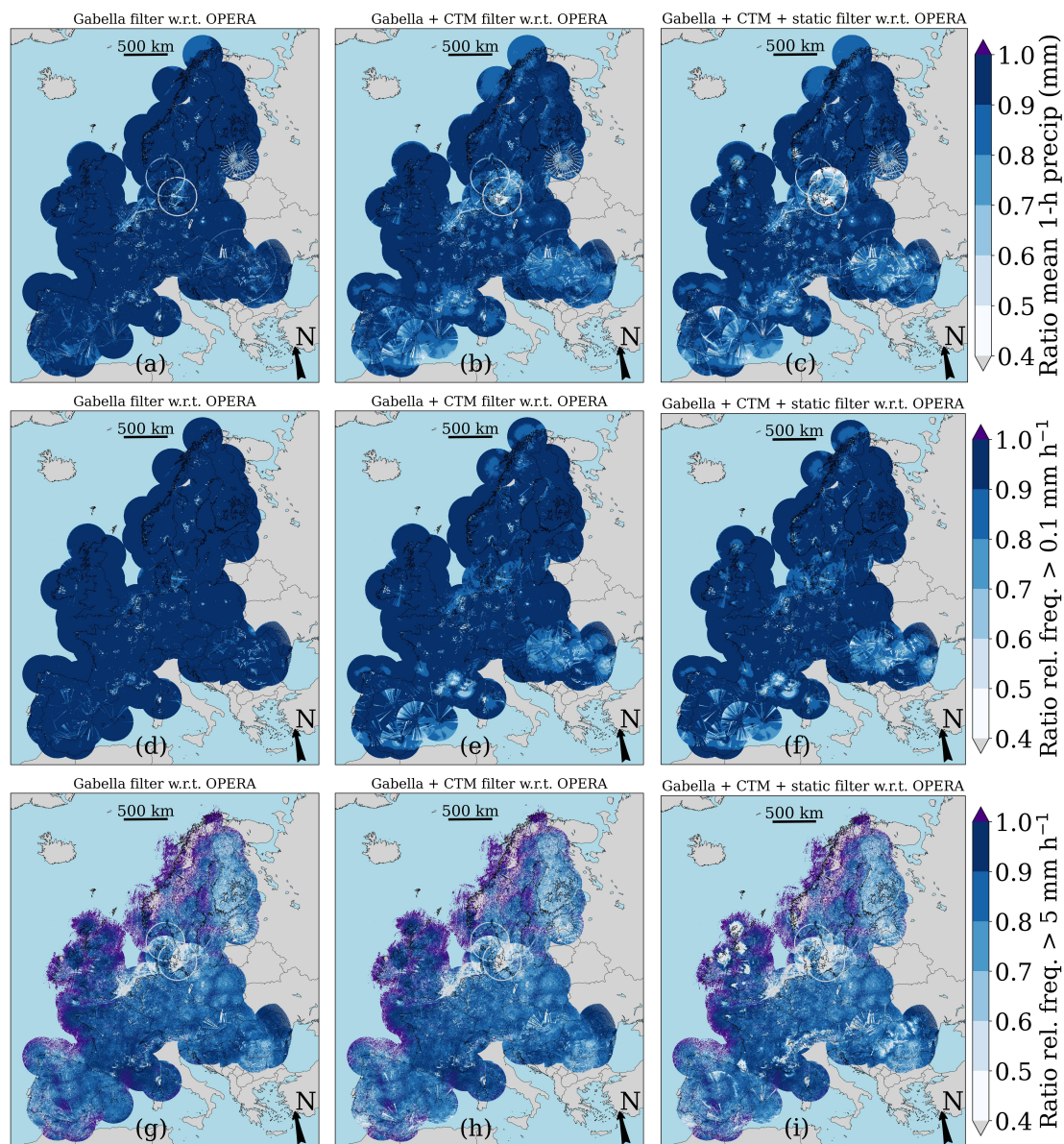
Figure A1. Comparison between 1-h precipitation accumulations from three datasets to study the effect of non-meteorological echo removal algorithms over the period 2013–2020. (a)–(c) Maps of the ratio of mean hourly precipitation with respect to the OPERA dataset, and (d)–(i) maps of the ratio of relative frequency of exceedance of 0.1 and 5 mm in an hour with respect to the OPERA dataset. The purple areas imply that the ratio is 1. The uncolored areas do not have data or have a relative frequency of 0 for one or both datasets. Map made with Natural Earth. Free vector and raster map data ©naturalearthdata.com.

Figure A2. Annual precipitation accumulations over the period 2013–2020 for EURADCLIM (4 km^2) and interpolated rain gauge observations (E-OBS version 25.0e; release April 2022; $0.1° \times 0.1°$, which is ~ 11 km in latitude and $\sim 4-9$ km in longitude, depending on the latitude). Coastlines are plotted in orange to ease the comparison between EURADCLIM and E-OBS, due to the coverage above open water by radars for which E-OBS does not provide precipitation estimates. Map made with Natural Earth. Free vector and raster map data ©naturalearthdata.com.

References

Al-Sakka, H., Boumahmoud, A.-A., Fradon, B., Frasier, S. J., and Tabary, P.: A new fuzzy logic hydrometeor classification scheme applied to the French X-, C-, and S-band polarimetric radars, J. Appl. Meteor. Climatol., 52, 2328–2344, https://doi.org/10.1175/JAMC-D-12-0236.1, 2013.

Allen, R. J. and DeGaetano, A. T.: Considerations for the use of radar-derived precipitation estimates in determining return intervals for extreme areal precipitation amounts, J. Hydrol., 315, 203–219, doi:10.1016/j.jhydrol.2005.03.028, 2005.

Barnes, S. L.: A technique for maximizing details in numerical weather map analysis, J. Appl. Meteor., 3, 396–409, 1964.

Barton, Y., Sideris, I., Raupach, T., Gabella, M., Germann, U., and Martius, O.: A multi-year assessment of sub-hourly gridded precipitation for Switzerland based on a blended radar—Rain-gauge dataset, Int. J. Climatol., 40, 5208–5222, https://doi.org/10.1002/joc.6514, 2020.

Benas, N., Finkensieper, S., Stengel, M., van Zadelhoff, G.-J., Hanschmann, T., Hollmann, R., and Meirink, J. F.: The MSG-SEVIRI-based cloud property data record CLAAS-2, Earth Syst. Sci. Data, 9, 415–434, https://doi.org/10.5194/essd-9-415-2017, 2017.

Berenguer, M., Sempere-Torres, D., Corral, C., and Sánchez-Diezma, R.: A fuzzy logic technique for identifying nonprecipitating echoes in radar scans, J. Atmos. Oceanic Technol., 23, 1157–1180, https://doi.org/10.1175/JTECH1914.1, 2006.

Berg, P., Christensen, O., Klehmet, K., Lenderink, G., Olsson, J., Teichmann, C., and Yang, W.: Summertime precipitation extremes in a EURO-CORDEX 0.11° ensemble at an hourly resolution, Nat. Hazards Earth Syst. Sci., 19, 957–971, https://doi.org/10.5194/nhess-19-957-2019, 2019.

Bližňák, V., Kašpar, M., and Müller, M.: Radar-based summer precipitation climatology of the Czech Republic, Int. J. Climatol., 38, 677–691, https://doi.org/10.1002/joc.5202, 2018.

Carey, L. D., Rutledge, S. A., Ahijevych, D. A., and Keenan, T. D.: Correcting propagation effects in C-band polarimetric radar observations of tropical convection using differential propagation phase, J. Appl. Meteor., 39, 1405–1433, https://doi.org/10.1175/1520-0450(2000)039<1405:CPEICB>2.0.CO;2, 2000.

Cornes, R. C., Van der Schrier, G., Van den Besselaar, E. J. M., and Jones, P. D.: An ensemble version of the E-OBS temperature and precipitation data sets, J. Geophys. Res.: Atmospheres, 123, 9391–9409, https://doi.org/10.1029/2017JD028200, 2018.

Crisologo, I., Vulpiani, G., Abon, C. C., David, C. P. C., Bronstert, A., and Heistermann, M.: Polarimetric rainfall retrieval from a C-band weather radar in a tropical environment (the Philippines), Asia-Pac. J. Atmos. Sci., 50(S), 43–55, https://doi.org/10.1007/s13143-014-0049-y, 2014.

De Vos, L. W., Leijnse, H., Overeem, A., and Uijlenhoet, R.: Quality control for crowdsourced personal weather stations to enable operational rainfall monitoring, Geophys. Res. Lett., 46, 8820–8829, https://doi.org/10.1029/2019GL083731, 2019.

Derrien, M. and Le Gléau, H.: MSG/SEVIRI cloud mask and type from SAFNWC, Int. J. Remote Sens., 26, 4707–4732, 2005.

Doviak, R. J. and Zrnić, D. S.: Doppler Radar and Weather Observations, Dover Publications, Inc., Mineola, New York, second edn., 1993.

Durrans, S. R., Julian, L. T., and Yekta, M.: Estimation of depth-area relationships using radar-rainfall data, J. Hydrol. Eng., 7, 356 – 367, doi:10.1061/(ASCE)1084–0699(2002)7:5(356), 2002.

Fabry, F.: Radar Meteorology: Principles and Practice, Cambridge University Press, Cambridge, U.K., https://doi.org/10.1017/CBO9781107707405, 2015.

Fabry, F., Meunier, V., Treserras, B. P., Cournoyer, A., and Nelson, B.: On the climatological use of radar data mosaics: possibilities and challenges, Bull. Amer. Meteor. Soc., 98, 2135–2148, https://doi.org/10.1175/BAMS-D-15-00256.1, 2017.

Finkensieper, S., Meirink, J.-F., van Zadelhoff, G.-J., Hanschmann, T., Benas, N., Stengel, M., Fuchs, P., Hollmann, R., and Werscheck, M.: CLAAS-2: CM SAF CLoud property dAtAset using SEVIRI - Edition 2, Satellite Application Facility on Climate Monitoring, https://doi.org/10.5676/EUM_SAF_CM/CLAAS/V002, 2016.

Frech, M., Hagen, M., and Mammen, T.: Monitoring the absolute calibration of a polarimetric weather radar, J. Atmos. Oceanic Technol., 34, 599–615, https://doi.org/10.1175/JTECH-D-16-0076.1, 2017.

Frederick, R. H., Myers, V. A., and Auciello, E. P.: Storm depth-area relations from digitized radar returns, Water Resour. Res., 13, 675–679, 1977.

Gabella, M. and Notarpietro, R.: Ground clutter characterization and elimination in mountainous terrain, in: Use of radar observations in hydrological and NWP models, pp. 305–311, Katlenburg-Lindau, Copernicus, https://iris.polito.it/handle/11583/1411995, 2002.

Garcia-Marti, I., Overeem, A., Noteboom, J. W., de Vos, L., de Haij, M., and Whan, K.: From proof-of-concept to proof-of-value: approaching third-party data to operational workflows of national meteorological services, Int. J. Climatol., 43, 275–292, https://doi.org/10.1002/joc.7757, 2023.

Goudenhoofdt, E. and Delobbe, L.: Evaluation of radar-gauge merging methods for quantitative precipitation estimates, Hydrol. Earth Syst. Sci., 13, 195–203, https://doi.org/10.5194/hess-13-195-2009, 2009.

Goudenhoofdt, E. and Delobbe, L.: Generation and verification of rainfall estimates from 10-yr volumetric weather radar measurements, J. Hydrometeor., 17, 1223–1242, https://doi.org/10.1175/JHM-D-15-0166.1, 2016.

Gourley, J. J., Tabary, P., and Parent du Chatelet, J.: A fuzzy logic algorithm for the separation of precipitating from nonprecipitating echoes using polarimetric radar observations, J. Atmos. Oceanic Technol., 24, 1439–1451, https://doi.org/10.1175/JTECH2035.1, 2007.

Graf, M., Chwala, C., Polz, J., and Kunstmann, H.: Rainfall estimation from a German-wide commercial microwave link network: optimized processing and validation for 1 year of data, Hydrol. Earth Syst. Sci., 24, 2931–2950, https://doi.org/10.5194/hess-24-2931-2020, 2020.

Graf, M., El Hachem, A., Eisele, M., Seidel, J., Chwala, C., Kunstmann, H., and Bárdossy, A.: Rainfall estimates from opportunistic sensors in Germany across spatio-temporal scales, J. Hydrol.: Regional Studies, 37, 1448–1463, https://doi.org/10.1016/j.ejrh.2021.100883, 2021.

Hazenberg, P., Torfs, P. J. J. F., Leijnse, H., Delrieu, G., and Uijlenhoet, R.: Identification and uncertainty estimation of vertical reflectivity profiles using a Lagrangian approach to support quantitative precipitation measurements by weather radar, J. Geophys. Res.: Atmospheres, 118, 10,243–10,261, https://doi.org/10.1002/jgrd.50726, 2013.

Heistermann, M., Jacobi, S., and Pfaff, T.: Technical Note: An open source library for processing weather radar data (*wradlib*), Hydrol. Earth. Syst. Sci., 17, 863–871, https://doi.org/10.5194/hess-17-863-2013, 2013.

Hitschfeld, W. and Bordan, J.: Errors inherent in the radar measurement of rainfall at attenuating wavelengths, J. Meteor., 11, 58–67, https://doi.org/10.1175/1520-0469(1954)011<0058:EIITRM>2.0.CO;2, 1954.

Holleman, I.: Bias adjustment and long-term verification of radar-based precipitation estimates, Meteor. Appl., 14, 195–203, https://doi.org/10.1002/met.22, 2007.

Huuskonen, A., Saltikoff, E., and Holleman, I.: The operational weather radar network in Europe, Bull. Amer. Meteor. Soc., 95, 897–907, https://doi.org/10.1175/BAMS-D-12-00216.1, 2014.

Jacobi, S. and Heistermann, M.: Benchmarking attenuation correction procedures for six years of single-polarized C-band weather radar observations in South-West Germany, Geomat. Nat. Haz. Risk, 7, 1785–1799, https://doi.org/10.1080/19475705.2016.1155080, 2016.

Kitchen, M. and Blackall, R. M.: Representativeness errors in comparisons between radar and gauge measurements of rainfall, J. Hydrol., 134, 13–33, 1992.

Klein Tank, A. and coauthors: Daily dataset of 20th-century surface air temperature and precipitation series for the European Climate Assessment, Int. J. Climatol., 22, 1441–1453, https://doi.org/10.1002/joc.773, 2002.

645 Klok, E. and Klein Tank, A.: Updated and extended European dataset of daily climate observation, Int. J. Climatol., 29, 1182–1191, https://doi.org/doi:10.1002/joc.1779, 2008.

KNMI: Precipitation - 5 minute precipitation accumulations from climatological gauge-adjusted radar dataset for The Netherlands (1 km, extended mask) in KNMI HDF5 format, retrieved July 2022, 2022.

Krause, J. M.: A simple algorithm to discriminate between meteorological and nonmeteorological radar echoes, J. Atmos. Oceanic Technol.,

650 33, 1875–1885, https://doi.org/10.1175/JTECH-D-15-0239.1, 2016.

Leijnse, H., Uijlenhoet, R., and Stricker, J. N. M.: Rainfall measurement using radio links from cellular communication networks, Water Resour. Res., 43, n/a–n/a, https://doi.org/10.1029/2006WR005631, w03201, 2007.

Lengfeld, K., Winterrath, T., Junghänel, T., Hafer, M., and Becker, A.: Characteristic spatial extent of hourly and daily precipitation events in Germany derived from 16 years of radar data, Meteorol. Z., 28, 363–378, https://doi.org/10.1127/metz/2019/0964, 2019.

655 Lengfeld, K., Walawender, E., Winterrath, T., and Becker, A.: CatRaRE: A Catalogue of radar-based heavy rainfall events in Germany derived from 20 years of data, Meteorol. Z., 30, 469–487, https://doi.org/0.1127/metz/2021/1088, 2021.

Lochbihler, K., Lenderink, G., and Siebesma, A. P.: The spatial extent of rainfall events and its relation to precipitation scaling, Geophys. Res. Lett., 44, 8629–8636, https://doi.org/10.1002/2017GL074857, 2017.

Marra, F. and Morin, E.: Use of radar QPE for the derivation of Intensity–Duration–Frequency curves in a range of climatic regimes, J.

660 Hydrol., 531, 427–440, https://doi.org/10.1016/j.jhydrol.2015.08.064, 2015.

McGraw, D., Nikolopoulos, E. I., Marra, F., and Anagnostou, E. N.: Precipitation frequency analyses based on radar estimates: An evaluation over the contiguous United States, J. Hydrol., 573, 299–310, https://doi.org/10.1016/j.jhydrol.2019.03.032, 2019.

Messer, H. A., Zinevich, A., and Alpert, P.: Environmental monitoring by wireless communication networks, Science, 312, 713, https://doi.org/10.1126/science.1120034, 2006.

665 Met Office: Cartopy: a cartographic python library with a Matplotlib interface, https://scitools.org.uk/cartopy, 2010 - 2015.

Michelson, D. B., Lewandowski, R., Szewczykowski, M., Beekhuis, H., Haase, G., Mammen, T., Faure, D., Simpson, M., Leijnse, H., and Johnson, D.: *EUMETNET OPERA weather radar information model for implementation with the HDF5 file format Version 2.3*, EUMETNET OPERA, available via https://www.eumetnet.eu/wp-content/uploads/2019/01/ODIM_H5_v23.pdf, 2019.

Mühlbauer, K., Heistermann, M., and Goudenhoofdt, E.: wradlib/wradlib: wradlib release v1.9.0 (1.9.0). Zenodo,

670 https://doi.org/10.5281/zenodo.4290240, 2020.

Nelson, B. R., Prat, O. P., Seo, D.-J., and Habib, E.: Assessment and implications of NCEP Stage IV quantitative precipitation estimates for product intercomparisons, Wea. Forecasting, 31, 371–394, https://doi.org/10.1175/WAF-D-14-00112.1, 2016.

NWC SAF: Algorithm Theoretical Basis Document for "Cloud Products" (CMa-PGE01 v3.2, CT-PGE02 v2.2 and CTTH-PGE03 v2.2), Tech. Rep. SAF/NWC/CDOP2/MFL/SCI/ATBD/01, Issue 3, Rev. 2.1, EUMETSAT Satellite Application Facility on Nowcasting and

675 Short range Forecasting, 2013.

OPERA: OPERA - Eumetnet, https://www.eumetnet.eu/activities/observations-programme/current-activities/opera/, retrieved June 2022, 2022.

Overeem, A.: EURADCLIM-tools (v.1.0), https://doi.org/10.5281/zenodo.7473816, 2022.

Overeem, A., Buishand, T. A., and Holleman, I.: Extreme rainfall analysis and estimation of depth-duration-frequency curves using weather

680 radar, Water Resour. Res., 45, n/a–n/a, https://doi.org/10.1029/2009WR007869, w10424, 2009a.

Overeem, A., Holleman, I., and Buishand, A.: Derivation of a 10-year radar-based climatology of rainfall, J. Appl. Meteor. Climatol., 48, 1448–1463, https://doi.org/10.1175/2009JAMC1954.1, 2009b.

Overeem, A., Buishand, T. A., Holleman, I., and Uijlenhoet, R.: Extreme value modeling of areal rainfall from weather radar, Water Resour. Res., 46, n/a–n/a, https://doi.org/10.1029/2009WR008517, w09514, 2010.

685 Overeem, A., Leijnse, H., and Uijlenhoet, R.: Two and a half years of country-wide rainfall maps using radio links from commercial cellular telecommunication networks, Water Resour. Res., 52, 8039–8065, https://doi.org/10.1002/2016WR019412, 2016.

Overeem, A., Uijlenhoet, R., and Leijnse, H.: Full-year evaluation of non-meteorological echo removal with dual-polarization fuzzy logic for two C-band radars in a temperate climate, J. Atmos. Oceanic Technol., 37, 1643–1660, https://doi.org/10.1175/JTECH-D-19-0149.1, 2020.

690 Overeem, A., de Vries, H., Al Sakka, H., Uijlenhoet, R., and Leijnse, H.: Rainfall-induced attenuation correction for two operational dual-polarization C-band radars in the Netherlands, J. Atmos. Oceanic Technol., 38, 1125–1142, https://doi.org/10.1175/JTECH-D-20-0113.1, 2021.

Overeem, A., van den Besselaar, E., van der Schrier, G., Meirink, J., van der Plas, E., and Leijnse, H.: EURADCLIM: The European climatological gauge-adjusted radar precipitation dataset (1-h accumulations), https://doi.org/10.21944/7ypj-wn68, 2022a.

695 Overeem, A., van den Besselaar, E., van der Schrier, G., Meirink, J., van der Plas, E., and Leijnse, H.: EURADCLIM: The European climatological gauge-adjusted radar precipitation dataset (24-h accumulations), https://doi.org/10.21944/1a54-gg96, 2022b.

Park, S., Berenguer, M., and Sempere-Torres, D.: Long-term analysis of gauge-adjusted radar rainfall accumulations at European scale, J. Hydrol., 573, 768–777, https://doi.org/10.1016/j.jhydrol.2019.03.093, 2019.

Project team ECA&D, Royal Netherlands Meteorological Institute KNMI: *European Climate Assessment & Dataset (ECA&D), Algo-*
700 *rithm Theoretical Basis Document (ATBD)*, December 9, 2021, Version 11, available via https://knmi-ecad-assets-prd.s3.amazonaws.com/documents/atbd.pdf, 2021.

Rauber, R. M. and Nesbitt, S. L.: Radar Meteorology: A First Course, John Wiley & Sons, Hoboken, NJ, U.S.A., https://doi.org/10.1002/9781118432662, 2018.

Ryzhkov, A. V. and Zrnic, D. S.: Radar Polarimetry for Weather Observations, Springer Nature Switzerland AG, Cham, Switzerland,
705 https://doi.org/10.1007/978-3-030-05093-1, 2019.

Saltikoff, E., Cho, J. Y. N., Tristant, P., Huuskonen, A., Allmon, L., Cook, R., Becker, E., and Joe, P.: The threat to weather radars by wireless technology, Bull. Amer. Meteor. Soc., 97, 1159–1167, https://doi.org/10.1175/BAMS-D-15-00048.1, 2016.

Saltikoff, E., Friedrich, K., Soderholm, J., Lengfeld, K., Nelson, B., Becker, A., Hollmann, R., Urban, B., Heistermann, M., and Tassone, C.: An overview of using weather radar for climatological studies: successes, challenges, and potential, Bull. Amer. Meteor. Soc., 100,
710 1739–1752, https://doi.org/10.1175/BAMS-D-18-0166.1, 2019a.

Saltikoff, E., Haase, G., Delobbe, L., Gaussiat, N., Martet, M., Idziorek, D., Leijnse, H., Novák, P., Lukach, M., and Stephan, K.: OPERA the radar project, Atmosphere, 10, https://doi.org/10.3390/atmos10060320, 2019b.

Skofronick-Jackson, G., Kirschbaum, D., Petersen, W., and et al.: The Global Precipitation Measurement (GPM) mission's scientific achievements and societal contributions: reviewing four years of advanced rain and snow observations., Q. J. R. Meteorol. Soc., 144, 27–48,
715 https://doi.org/10.1002/qj.3313, 2018.

Sun, Q., Miao, C., Duan, Q., Ashouri, H., Sorooshian, S., and Hsu, K.-L.: A review of global precipitation data sets: data sources, estimation, and intercomparisons, Rev. Geophys., 56, 79–107, https://doi.org/10.1002/2017RG000574, 2018.

Tabary, P., Vulpiani, G., Gourley, J. J., Illingworth, A. J., Thompson, R. J., and Bousquet, O.: Unusually high differential attenuation at C Band: results from a two-year analysis of the French Trappes polarimetric radar data, J. Appl. Meteor. Climatol., 48, 2037–2053, https://doi.org/10.1175/2009JAMC2039.1, 2009.

720

Testud, J., Le Bouar, E., Obligis, E., and Ali-Mehenni, M.: The rain profiling algorithm applied to polarimetric weather radar, J. Atmos. Oceanic Technol., 17, 332–356, https://doi.org/10.1175/1520-0426(2000)017<0332:TRPAAT>2.0.CO;2, 2000.

Van de Beek, C. Z., Leijnse, H., Torfs, P. J. J. F., and Uijlenhoet, R.: Seasonal semi-variance of Dutch rainfall at hourly to daily scales, Adv. Water Resour., 45, 76–85, https://doi.org/10.1016/j.advwatres.2012.03.023, 2012.

725

Van der Plas, E., Schmeits, M., Hooijman, N., and Kok, K.: A comparative verification of high-resolution precipitation forecasts using model output statistics, Mon. Wea. Rev., 145, 4037–4054, https://doi.org/10.1175/MWR-D-16-0256.1, 2017.

Vulpiani, G., Montopoli, M., Passeri, L. D., Gioia, A. G., Giordano, P., and Marzano, F. S.: On the use of dual-polarized C-band radar for operational rainfall retrieval in mountainous areas, J. Appl. Meteor. Climatol., 51, 405–425, https://doi.org/10.1175/JAMC-D-10-05024.1, 2012.

730

Winterrath, T., Brendel, C., Hafer, M., Junghänel, T., Klameth, A., Lengfeld, K., Walawender, E., Weigl, E., and Becker, A.: *RADKLIM Version 2017.002: Reprocessed gauge-adjusted radar data, one-hour precipitation sums (RW). – Radar-based Precipitation Climatology Version 2017.002*, https://doi.org/10.5676/DWD/RADKLIM_RW_V2017.002, 2018.

Wradlib: wradlib.clutter.filter_gabella | wradlib, https://docs.wradlib.org/en/stable/generated/wradlib.clutter.filter_gabella.html?highlight=gabella, retrieved December 2021, 2021.

735

Wradlib: wradlib.clutter.histo_cut | wradlib, https://docs.wradlib.org/en/stable/generated/wradlib.clutter.histo_cut.html, retrieved June 2022, 2022.